

AN ESR STUDY OF  $\text{Zn}_2\text{P}_2\text{O}_7$ : Mn AND  
 $\text{Zn}_2\text{P}_2\text{O}_7$ : Cu BETWEEN 20 AND 200°C

AN ESR STUDY OF  $Zn_2P_2O_7$ : Mn AND  
 $Zn_2P_2O_7$ : Cu BETWEEN 20 AND 200°C

BY

JOHN GILBERT CHAMBERS, B.Sc., M.A.

A Thesis

Submitted to the Faculty of Graduate Studies  
in Partial Fulfilment of the Requirements  
for the Degree  
Doctor of Philosophy

McMaster University

October, 1963

DOCTOR OF PHILOSOPHY (1963)  
(Physics)

McMASTER UNIVERSITY  
Hamilton, Ontario

TITLE: An ESR Study of  $Zn_2P_2O_7$ : Mn And  $Zn_2P_2O_7$ : Cu Between  
20 and 200°C

AUTHOR: John Gilbert Chambers, B.Sc. (Acadia University)  
M.A. (Wesleyan University)

SUPERVISORS: Professors C. Calvo, A. B. McLay and H. E. Petch

NUMBER OF PAGES: vii, 74

CONTENTS: Single crystals of  $Zn_2P_2O_7$  containing 0.1% by weight  
of manganese impurity or 0.04% by weight of copper  
impurity were studied by means of electron spin  
resonance techniques from room temperature up to  
about 200°C.

The existence of a phase transition at about  
132°C in  $Zn_2P_2O_7$  was confirmed and a new phase,  
existing between 132°C and 155°C was found. The  
space group of the unit cell in this phase was deduced  
from the esr measurements. The spin Hamiltonian  
parameters were measured in the three phases and a  
discussion of their significance in terms of current  
theories of the zero field splitting of the ground  
state of S-state ions is given.

### ACKNOWLEDGEMENTS

The author wishes to express his sincere gratitude to Professors C. Calvo, A. B. McLay and H. E. Petch for their guidance and help throughout the course of this research. Thanks are also extended to Professor W. R. Datars for helpful discussions and his generosity in allowing the use of the 0.8 cm. esr spectrometer used in this work.

The research was made possible through grants-in-aid from the Ontario Research Foundation to Professors H. E. Petch and A. B. McLay.

## TABLE OF CONTENTS

	<u>SUBJECT</u>	<u>PAGE</u>
CHAPTER I	Introduction	1
1	S-State Ions	1
2	The Phase Transition in $Zn_2P_2O_7$	3
CHAPTER II	Theory	5
1	The Spin Hamiltonian for $Cu^{++}$	5
2	The Spin Hamiltonian for $Mn^{++}$	7
3	S-State Ions	8
4	Comparison of Theory and Experiment for Axial Symmetry	12
5	Electron Exchange Effects	14
6	Energy Levels of the Spin Hamiltonian for $Mn^{++}$	16
CHAPTER III	Crystallography and Phase Relationships in the Divalent Phosphates	19
CHAPTER IV	Experimental Procedure and Results	24
1	The ESR Spectrometers	24
2	The 3 cm. Sample Holder and Oven	25
3	The 0.8 cm. Sample Holder and Oven	26
4	Alignment of the Sample	28
5	Spectra of $Cu^{++}$ and $Mn^{++}$ at Various Temperatures	30
6	Angular Variations of the Magnetic Axes	32
7	Measurement of the Line Positions	34
8	Determination of the Spin Hamiltonian Parameters for $Mn^{++}$	37

	<u>SUBJECT</u>	<u>PAGE</u>
9	Effects Arising From Changes in the Magnetic Axes Directions	53
10	The Spin Hamiltonian Parameters for $\text{Cu}^{++}$	55
11	The Directions of the Magnetic Axes in the Crystal	57
CHAPTER V	Discussion of Results and Conclusions	58
1	The Relation Between the Electric Field Gradient and the Axial Splitting Parameter D	58
2	The Intermediate Phase	61
3	The Parameters A and g	64a
4	Future Experiments	64a

List of Tables

<u>Table</u>	<u>Subject</u>	<u>Page</u>
I	Zn <sub>2</sub> P <sub>2</sub> O <sub>7</sub> Crystallographic Data	23
II	Position of esr Lines in Gauss in Mn: Zn <sub>2</sub> P <sub>2</sub> O <sub>7</sub>	38
III	Position of esr Lines in Gauss in Cu: Zn <sub>2</sub> P <sub>2</sub> O <sub>7</sub>	45
IV	Spin Hamiltonian Parameters for Mn <sup>++</sup> at Room Temperature, 136°C and 184°C	50
V	Hyperfine Splitting of Fine Structure Lines at 184°C	52
VI	Spin Hamiltonian Parameters for Cu <sup>++</sup> at 136°C and 181°C	56
VII	Values of the Matrix Element $\langle \alpha^n   H_i   \alpha^n \rangle$	67
VIII	Atom Positions in $\beta$ -Zn <sub>2</sub> P <sub>2</sub> O <sub>7</sub>	69
IX	Field Gradients in $\beta$ -Zn <sub>2</sub> P <sub>2</sub> O <sub>7</sub>	70
X	Atom Positions in Mn <sub>2</sub> P <sub>2</sub> O <sub>7</sub>	71
XI	Field Gradients in Mn <sub>2</sub> P <sub>2</sub> O <sub>7</sub>	71

List of Illustrations

<u>Figure</u>	<u>Subject</u>	<u>Page</u>
1.	Crystal Field Splitting of the Energy Levels of the $\text{Cu}^{++}$ D Ion	6
2.	Terms Arising From the $3d^5$ Configuration	10
3.	Optical Absorption Measurements in (a) $\text{MnO}$ and (b) $\text{MnF}_2$	11
4.	Axial Splitting Parameter D of $\text{Fe}^{3+}$ in various crystals (a) $\text{A}_2^{\circ}$ and (b) the quadrupole coupling constant eq Q/n	14
5.	The Crystal Structure of $\beta\text{-Zn}_2\text{P}_2\text{O}_7$	22
6.	The Cation Environment in $\beta\text{-Zn}_2\text{P}_2\text{O}_7$	23
7.	The Block Diagram of the 3 cm. ESR Spectrometer	25
8.	The 3 cm. Sample Holder Design	26
9.	The 3 cm. Microwave Cavity and Oven Assembly	27
10.	The 0.8 cm. Sample Holder and Oven Assembly	28
11.	The ESR Spectra of $\text{Cu}^{++}$ in $\text{Zn}_2\text{P}_2\text{O}_7$ With H//z-axis at Various Temperatures	31
12.	ESR Spectra of $\text{Cu}^{++}$ in $\text{Zn}_2\text{P}_2\text{O}_7$ With H//x and H//y at Various Temperatures	32
13.	ESR Spectra of $\text{Mn}^{++}$ in $\text{Zn}_2\text{P}_2\text{O}_7$ With H//y at Various Temperatures	33
14.	Temperature Variation of the Axial Splitting Parameter for $\text{Mn}^{++}$ in $\text{Zn}_2\text{P}_2\text{O}_7$	52
15.	Temperature Variations of the Splitting of the $\text{Cu}^{++}$ Spectra With H//z	58

## CHAPTER I

### INTRODUCTION

In the year immediately following the first successful electronic spin resonance (esr) experiment by Zavoisky (1945), much of the experimental and theoretical effort was directed toward an understanding and explanation of the resonance spectra themselves. Very soon, enough of the general features of these spectra were understood to allow the use of esr as a tool for the investigation of the electronic properties of liquids and solids.

Notwithstanding the quite substantial progress that has been made since that time in the theoretical interpretation of the esr spectra, many details, and in some cases major points, are not understood. One of the areas in which there is a gap between theory and experiment is the behavior of the energy levels of an S-state ion when it is incorporated in a crystal lattice.

#### 1.1 S-State Ions

When a free electron is subjected to an electric field one sees no effect on the Zeeman splitting of the magnetic spin energy levels. In contrast, when these spin levels are associated with an electron or electrons of a paramagnetic ion, an electric field influences the magnetic sub-levels via

the spin-orbit coupling. For most ions this mechanism is sufficient to account for the magnitude of observed splittings. Since S-state ions have zero electronic angular momentum one would expect no splitting of the magnetic sub-levels in an electric field. However, quite large splittings (of the order of  $0.1 \text{ cm}^{-1}$ ) have been observed in some cases. In attempts to explain this splitting, a number of mechanisms have been proposed which admix higher states with the ground state. None of these seem adequate, at least in their present formulation, to explain the observed effects.

Calculations based on an S-state ion in an environment of ligands characterized by point charges have been carried out for two types of cation environment; one in which the ion is situated at a lattice site of cubic symmetry, and the other in a lattice which has been distorted from cubic symmetry by an elongation or compression along a symmetry axis. In the latter case, the parameter that is calculated is the axial splitting parameter D. Previous to the present study, values of D for  $\text{Mn}^{++}$  have been usually of the order of 200 gauss and in a few instances up to about 450 gauss. In the present study of  $\text{Mn}^{++}$  in  $\text{Zn}_2\text{P}_2\text{O}_7$  values of D have been found which vary between 612 and 1319 gauss depending on the temperature and type of cation site.

Thus an esr study of this crystal and its analogues would provide data useful in studying the relationship of the D value of  $\text{Mn}^{++}$  to crystalline parameters.

## 1.2 The Phase Transition in $Zn_2P_2O_7$

One way of studying the effect of the environment on the energy levels of the ion is to change the environment slightly and observe the change in the esr spectrum. It sometimes happens that only slight structural changes occur when a crystal passes through a reversible phase transition. Such a transition has been observed to occur in  $Zn_2P_2O_7$  at  $132 \pm 8^\circ\text{C}$  (Katnack and Hummel, 1958) and in  $Mg_2P_2O_7$  at  $68^\circ\text{C}$  (Roy, Middlesworth, and Hummel, 1948).

In addition the phosphates in general have been of interest because of their luminescent behavior when activated with suitable ions. This interest has led to a study of the phase relationships in these materials. In particular some of the divalent pyrophosphates show a marked similarity in structure and phase behavior.

A detailed knowledge of the structures of the different phases of these pyrophosphates is undoubtedly necessary to the elucidation of the mechanisms involved in these transitions. At present the determination of the high temperature  $\beta$  phase of  $Zn_2P_2O_7$  has been completed. This present study was undertaken to provide information about the phase transition additional to that obtainable from x-ray analysis.  $Mn^{++}$  and  $Cu^{++}$  were the paramagnetic ions used because (a) the  $Mn^{++}$  is sensitive to small structural changes and the spectrum is easy to observe, (b) the observed behavior of the  $Mn^{++}$  spectrum at the phase transition suggested the need for a second paramagnetic ion to ensure that this behavior was

characteristic of the bulk material rather than the  $Mn^{++}$  ions, (c) the  $Cu^{++}$  Spectrum is simple, and (d)  $\beta - Cu_2 P_2 O_7$  and  $\beta - Mn_2 P_2 O_7$  are isomorphic to the crystals under study.

In summary then, the motivation for this investigation was two-fold. The first motive was to provide data which would extend the range of experimentally observed D values for  $Mn^{++}$  and which would serve as a first step in the esr study of some isostructural or otherwise related phosphate compounds. Because of the intended use of this data a somewhat extended discussion of the present state of the theory of S-state ions in crystals seemed in order and this is presented in Chapter II. The second motive was to further investigate the interesting behavior observed in preliminary experiments of the esr spectra of  $Mn^{++}$  in  $Zn_2 P_2 O_7$  above the phase transition at  $132^\circ C$ .

## CHAPTER II

### THEORY

#### 1. The Spin Hamiltonian for $\text{Cu}^{++}$

The ground state of the free  $\text{Cu}^{++}$  ion is  $3d^9 \ ^2D_{5/2}$ . In the solid state this ion is acted upon by the crystalline electric field. The effect of this field on the energy levels of the ion is illustrated in figure 1. We neglect, for the moment, the spin-orbit coupling, so that the  $^2D$  state of the free ion has five-fold degeneracy. In a crystal where the environment of the  $\text{Cu}^{++}$  has cubic symmetry the  $^2D$  level is split into two levels, separated by about  $10^4 \text{ cm}^{-1}$  in energy. If the symmetry is lower these two levels can be further split as shown. The effect of this last splitting is to leave the lowest level orbitally non-degenerate. This is called the "quenching out" of the orbital angular momentum in the iron group ions and, because it is only this lowest level that is appreciably populated at room temperature, results in the well-known "spin-only" paramagnetism of this group of ions.

This same effect allows the Zeeman splitting of the ground state in a magnetic field to be described by what is called a spin Hamiltonian. To see how this spin Hamiltonian arises we write down the normal Hamiltonian for the system of the ion in a crystal subjected to a magnetic field.

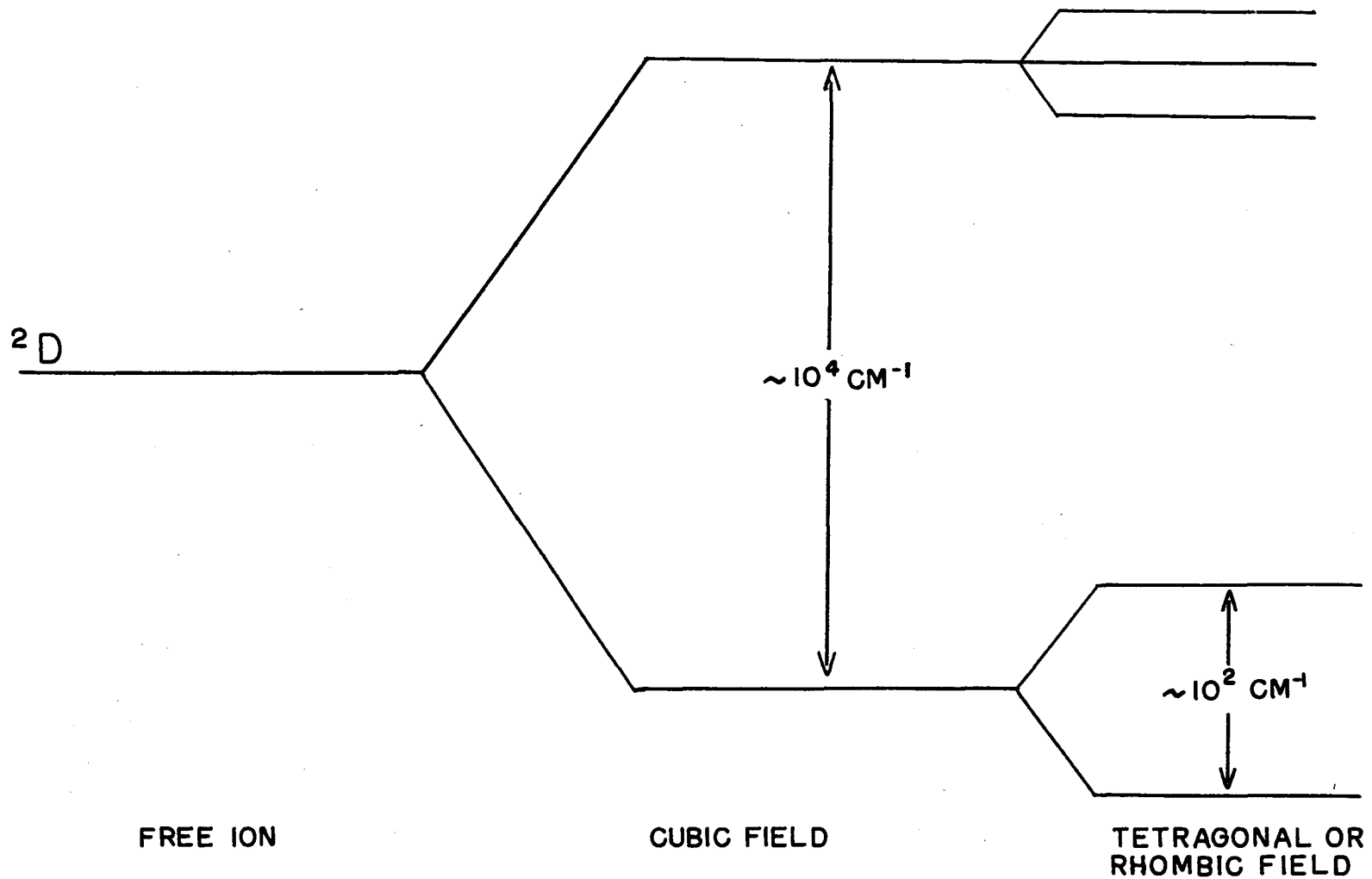


FIG. 1. CRYSTAL FIELD SPLITTING OF THE ENERGY LEVEL OF THE  $\text{Cu}^{++} 2D$  ION

$$\mathcal{H} = \sum_i \left( \frac{p_i^2}{2m} + \frac{Ze^2}{r_i} \right) + \sum_{i>j} \frac{e^2}{r_{ij}} + V_{\text{crystal}} + \lambda \vec{L} \cdot \vec{S} + \beta \vec{H} \cdot (\vec{L} + 2\vec{S}) + \beta \vec{H} \cdot (\vec{L} + 2\vec{S}) + V_{\text{nuclear}} \quad (2.1)$$

The first three terms are the coulomb interactions among the electrons and the nucleus and leave the ion in the  $^2D$  state shown in figure 1.  $V_{\text{crystal}}$  represents the effect of the crystalline electric field.  $\lambda \vec{L} \cdot \vec{S}$  is the spin-orbit interaction, and  $\beta \vec{H} \cdot (\vec{L} + 2\vec{S})$  is the interaction of the electronic moments with the magnetic field.  $V_{\text{nuclear}}$  represents interactions which are present when the nucleus in question has a magnetic moment. We have neglected the small spin-spin interactions. Fortunately, for ions of the iron group the various interactions, considering the coulomb interactions as one, decrease in size by at least an order of magnitude, in the sequence written in equation (2.1). This means that in finding the energy levels of the Hamiltonian each interaction can be considered as a perturbation on the preceding ones. As pointed out above, the first two interactions produce the splitting shown in figure 1. The "quenching out" of the electronic angular momentum leaves only  $2\beta \vec{H} \cdot \vec{S}$  as the interaction of the electronic magnetic moments with the magnetic field. The effect of the spin-orbit coupling is to mix some of the higher  $^2D$  wave functions with the ground state wave function. For  $\text{Cu}^{++}$  this results in a change in the spectroscopic splitting factor from its free-spin value. Instead of writing the magnetic

interaction term as  $2\beta \vec{H} \cdot \vec{S}$ , it becomes  $g\beta \vec{H} \cdot \vec{S}$ , where  $g$  is now a tensor quantity to account for the directional effects of the crystal lattice on the orbital angular momentum.

Finally, the nuclear interaction term includes the hyperfine interaction between the electronic and nuclear moments, the quadrupole interaction, and the direct magnetic interaction of the nuclear moment with the magnetic field. Only the first of these is large enough to be significant in the present case. This interaction can be written as  $A\vec{I} \cdot \vec{S}$ , where  $A$  is a tensor quantity.

Thus the net result of this quenching of the orbital angular momentum and of the fact that only the ground state in figure 1 is appreciably occupied at ordinary temperatures is that the simple "spin Hamiltonian"

$$\mathcal{H} = g\beta \vec{H} \cdot \vec{S} + A\vec{I} \cdot \vec{S} \quad (2.2)$$

can be used to describe the Zeeman splitting of the ground state of the  $\text{Cu}^{++}$  in a crystal. The nuclear spin  $I$  of the copper nucleus is  $\frac{3}{2}$  and the ground state spin is  $\frac{1}{2}$ . Since the selection rules are  $\Delta M_I = 0$  and  $\Delta M_S = 1$  this results in a spectrum of four lines with equal spacing  $A$ .

## 2. The Spin Hamiltonian for $\text{Mn}^{++}$

Although the spin Hamiltonian (2.2) is appropriate for  $S = \frac{1}{2}$ , additional terms are necessary if  $S$  is greater than  $\frac{1}{2}$ . The admixture of higher states into the ground state by the spin-orbit interaction results in a Stark splitting of the magnetic sub-levels even in zero magnetic field. For

this reason these splittings are called zero-field splittings. If the crystalline electric field has axial symmetry, a term  $DS_z^2$  must be added and if the symmetry is rhombic or lower an additional term  $E(S_x^2 - S_y^2)$  is necessary. Thus, under these conditions, the spin-Hamiltonian (2.2) becomes

$$H = g\beta \vec{H} \cdot \vec{S} + DS_z^2 + E(S_x^2 - S_y^2) + A\vec{I} \cdot \vec{S}. \quad (2.3)$$

In the case of  $Mn^{++}$ , however, there is the additional complication that the ground state of the free ion is an S-state. This means that there is no angular momentum and that those terms in the spin Hamiltonian which arise from the combined effect of the spin-orbit coupling and the crystalline electric field should not be present. Also, since the S-state results from d electrons outside closed shells little hyperfine interaction is expected. That is, the spin Hamiltonian should have the simple form

$$H = g\beta \vec{H} \cdot \vec{S}$$

In fact, quite large hyperfine interactions and zero field splittings are observed, and it turns out that the  $Mn^{++}$  spectra can be adequately described by the spin Hamiltonian (2.3).

### 3. S-State Ions

Since the  $Mn^{++}$  spectra can not be explained on the same basis as that described above for  $Cu^{++}$ , it is necessary to look for other mechanisms which could produce these effects. It has been proposed by Abragam (1950) that the anomalous hyperfine splitting arises from some admixture of the configuration  $3s3d^5 4S$  with the  $3s^2 3d^5$  configuration of  $Mn^{++}$ .

Later calculations (Heine, 1957; Wood and Pratt, 1957) indicate that there are also contributions from the closed  $3s^2$ ,  $2s^2$ , and  $1s^2$  shells arising from a polarization of these shells by the  $3d$  electrons. The situation is not completely resolved because of the difficulty of the calculations.

The situation is even less clear with regard to the fine structure splitting. Since the crystalline field cannot influence a pure S-state there must be some mixture of higher states in the ground state. The manner in which the admixture of these higher terms split the ground state is a formidable theoretical problem. Since the most serious attempts at solution have been made for the case of cubic symmetry, a brief discussion of the cubic splitting parameter "a" will be given as an introduction to the axially symmetric case. For S-state ions the Jahn-Teller effect does not apply, and it is quite common to find such ions in sites of cubic symmetry. In this case the axial terms in the spin-Hamiltonian (2.3) are absent. A much smaller splitting is found to occur which can be described by a term  $\frac{a}{6}(S_x^4 + S_y^4 + S_z^4)$  in the spin-Hamiltonian.

The calculated terms arising from the  $3d^5$  configuration of the free  $Mn^{++}$  ion are shown in figure 2. The free ion spectra are characterized by the parameters  $\lambda$ , B, and C, where  $\lambda$  is the spin-orbit coupling constant, and B and C are defined by

$$B = F_2 - 5F_4$$

$$C = 35F_4$$

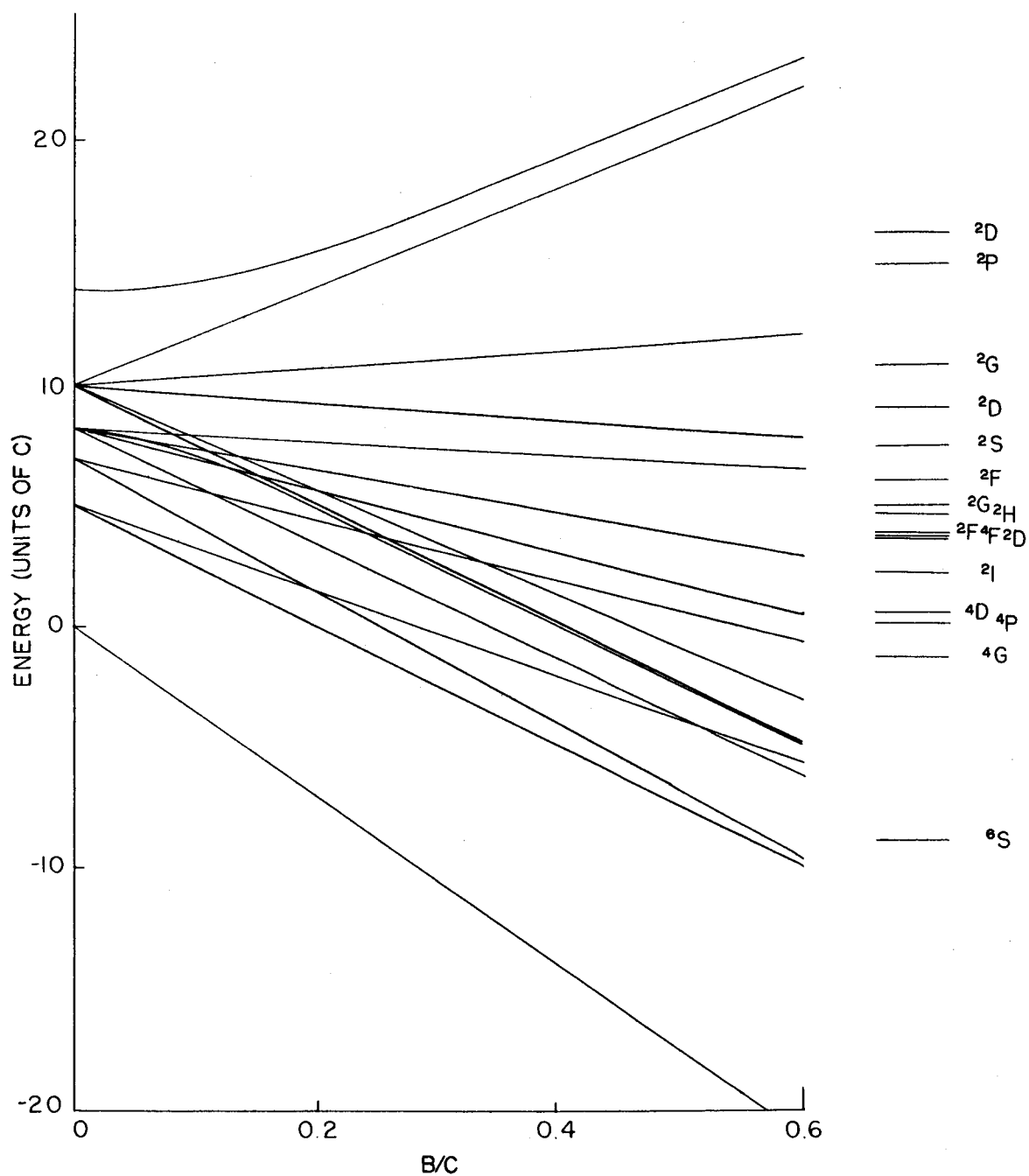


FIG. 2. TERMS ARISING FROM THE  $3d^5$  CONFIGURATION

The  $F_k$  are the Slater-Condon (Griffith, 1961) parameters involving the radial coulomb integrals. The energies in figure 2 are calculated in terms of  $C$  and are plotted against  $B/C$ . The value of  $B/C$  for the free ion is calculated to be approximately 0.25 and found experimentally to be 0.35. In a solid,  $MnO$  it is found to be about 0.25 (Pratt and Coelho, 1959). The energy levels for  $B/C = 0.25$  are shown at the right of figure 2. The crystal field splits and changes the energies of the terms shown in figure 2 in the manner shown in figure 3. The optical measurements shown in figure 3(a) were made by Pratt and Coelho (1959). To illustrate the variations of these splitting in different solids optical measurements made on  $MnF_2$  (Stout, 1959) are shown in figure 3(b). Terms arising from the excited  $3d^4 4s$  configuration lie higher than these quartets, the  ${}^6D_{5/2}$  state of the free ion being  $63285.2 \text{ cm}^{-1}$  above the  ${}^6S_{5/2}$  ground state.

Perturbations of at least fifth order involving combinations of the spin-orbit coupling, the spin-spin coupling, and the cubic crystalline field are required to split this ground state (Van Vleck, 1935). Because of the large number of terms in the  $d^5$  configuration alone, there will be many such perturbations possible. Watanabe (1957) lists twelve of these perturbations involving only the quartet terms shown in figure 2, assuming that contributions from the  $3d^5$

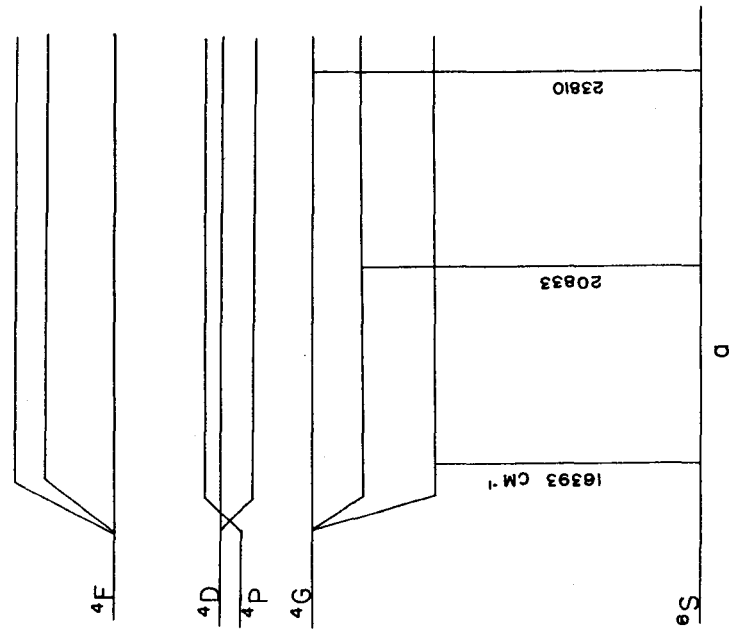
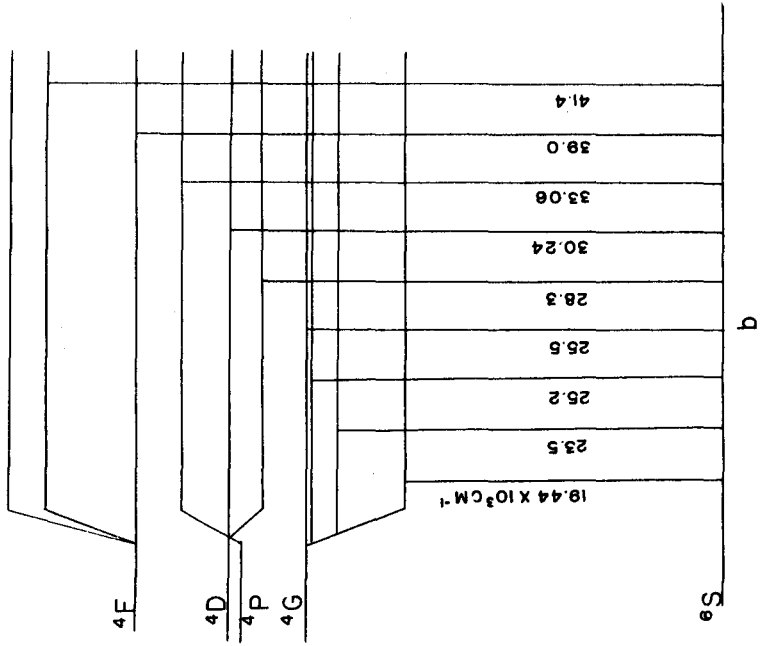


FIG. 3. OPTICAL ABSORPTION MEASUREMENTS IN (a)  $\text{MnO}$  AND (b)  $\text{MnF}_2$

doublet terms and terms of higher configurations are small because of their higher energies. In a more recent calculation Gabriel, Johnston and Powell (1961) consider all the contributions from the  $3d^5$  configuration for  $Mn^{++}$  in  $MnO$  and find that inclusion of the higher doublets increases the calculated value of "a" by two orders of magnitude. The results of this last calculation are not conclusive because the parameters B, C, and  $\lambda$  for  $Mn^{++}$  in  $MgO$  are not known. The best that can be said is that the calculated value of "a" can be made to agree with the experimental value for plausible values of B, C, and  $\lambda$ .

The situation is even less settled when the  $Mn^{++}$  site has only axial symmetry. In this case the zero field splitting is described by the term  $DS_2^2$  in the spin-Hamiltonian. The perturbation need now only be of the second order in spin to contribute to the splitting of the ground state. To date there have been four types of mechanisms proposed for  $Mn^{++}$ ; a second order perturbation involving the excited configuration  $3d^4 4s$ , linear in spin-spin coupling and the axial crystal field  $V_{ax}$  (Pryce 1950), a fourth order perturbation involving quartet terms of the  $3d^5$  configuration and quadratic in both spin-orbit coupling and  $V_{ax}$  (Watanabe, 1957), and two more terms, linear in  $V_{ax}$  and of the third order in spin variables (Germanier, Gainon, and Lecroix, 1962). No contributions from the doublet terms in the  $3d^5$  configuration have been considered.

A number of parameters have been used to denote the axial crystal field and it is worthwhile digressing for a moment to define them. In the point charge model the crystal field potential may be written

$$V = A_2^{\circ} r^2 Y_2^{\circ} + A_4^{\circ} r^4 [Y_4^{\circ} + (\frac{5}{14})^{1/2} (Y_4^4 + Y_4^{-4})] + \dots$$

where the  $Y_n^m$  are spherical harmonics. The first term is referred to as  $V_{ax}$ .  $A_2^{\circ}$  is also used as a measure of the axial field, and Watanabe uses a parameter  $\Delta$  defined by

$$\Delta = \frac{1}{4} \left( \frac{5}{\pi} \right)^{1/2} \langle r^2 \rangle A_2^{\circ}$$

where  $\langle r^2 \rangle$  is the average value of  $r^2$ .

#### 4. Comparison of Theory and Experiment for Axial Symmetry

The several attempts that have been made to match theory and experiment for axially symmetric cases serve to emphasize the uncertain state of the theory. A number of parameters appear in the theoretical expressions for  $D$  for which appropriate values are not known, and therefore the emphasis has been on the study of the variation of  $D$  with  $V_{ax}$ , rather than on the absolute values of  $D$ .

The proposed contributions to  $D$  are either linear or quadratic in  $V_{ax}$ , so that the general relationship is of the form

$$D = C_1 V_{ax} + C_2 V_{ax}^2.$$

Even though the magnitudes of the constants  $C_1$  and  $C_2$  are uncertain, one might expect a plot of  $D$  against  $V_{ax}$  to show a parabolic relationship which agrees at least with the

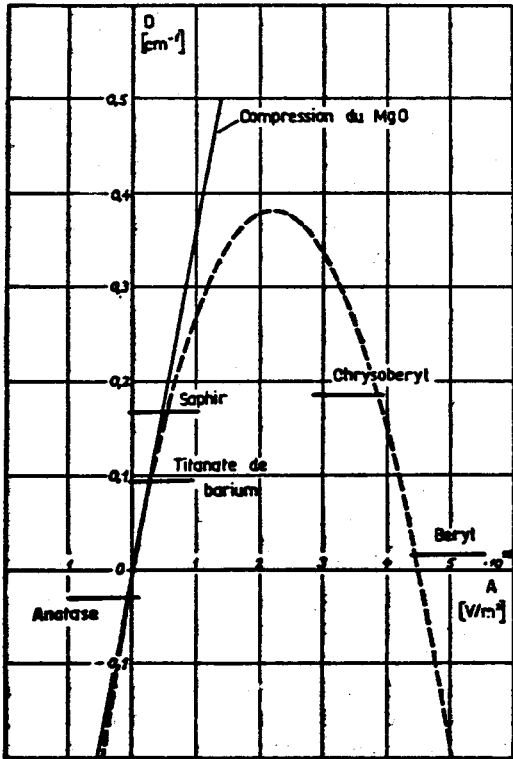
calculated signs of  $C_1$  and  $C_2$ . Unfortunately there is not complete agreement about the results of these calculations. Watanabe (1957) finds  $C_1$  to be positive and  $C_2$  negative. Germanier, et al (1962) find  $C_1$  to be negative because of the additional contributions that they postulate and disagree with Watanabe on the sign of  $C_2$ . Friedman (Nicholson and Burns, 1963) has confirmed this part of Watanabe's results.

The experimental evidence is also inconclusive. Germanier, et al (1962) have calculated  $A_2^0$  in crystals in which D has been measured for  $Fe^{3+}$ . Their results taken from their paper are shown in figure 4(a). The sign of  $C_1$  is positive and of  $C_2$  is negative for this parabola, in disagreement with their calculated values. Also the experimental values are two orders of magnitude larger in size than the calculated values.

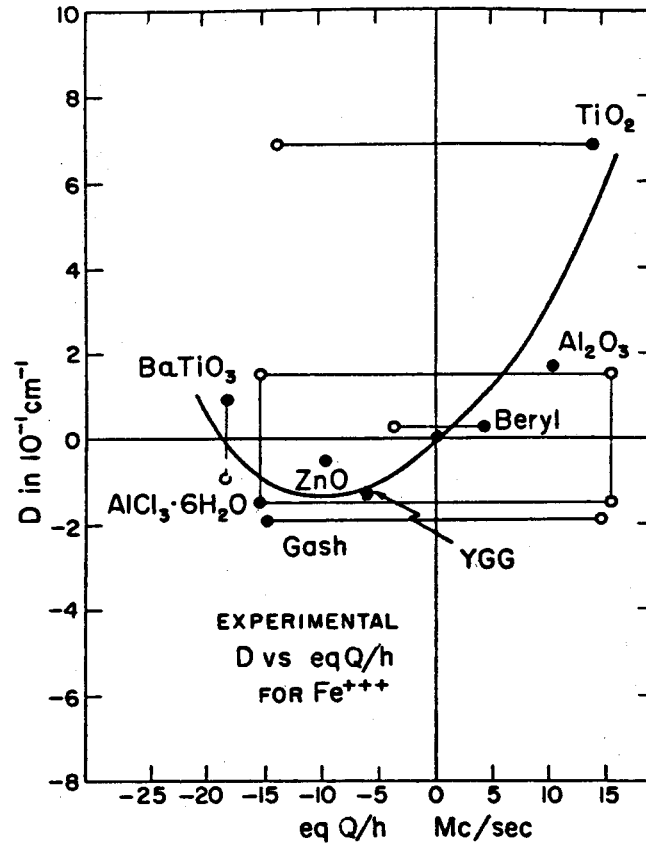
Quite different results have been obtained by Nicholson and Burns (1963). They used the Mössbauer absorption technique to measure the quadrupole coupling constant, eq  $Q/h$ , of  $Fe^{+++}$  in a number of materials.  $Q$  is the quadrupole constant of the  $Fe^{+++}$  nucleus and  $q$  is the electric field gradient at the nucleus. In the case of axial symmetry this field gradient can be written

$$q = (1 - \gamma_{\infty}) q_u = (1 - \gamma_{\infty}) \left(\frac{5}{\pi}\right)^{1/2} A_2^0$$

(Bersohn, 1958) where  $\gamma_{\infty}$  is the antishielding factor which accounts for the effect of the polarization of the electrons of the ion in question and  $q_u$  is the unshielded electric field gradient at the ion. The results of these measurements,



a



b

FIG. 4 . AXIAL SPLITTING PARAMETER  $D$  OF  $\text{Fe}^{3+}$  IN VARIOUS CRYSTALS Vs (a)  $A_2^0$  AND (b) THE QUADRUPOLE COUPLING CONSTANT  $eqQ/h$ .

also from the original paper, are shown in figure 4(b). The open circles indicate that eq Q/h is unreliable or the sign of D is unknown. In these cases signs were chosen to give a single-valued relationship between D and eq Q/h. For this parabola,  $C_2$  is negative. The scatter of the points is large, however, and the curvature is primarily given by  $Fe^{3+}$  in  $TiO_2$ . Since  $Fe^{3+}$  substitutes for  $Ti^{4+}$  in  $TiO_2$  it would not be surprising if this point is particularly unreliable.

It should be pointed out that all of the uncertainty in these studies does not lie in the calculations of D. Both of the experiments discussed are performed on ions which are impurities in their host lattices, and in some cases the  $Fe^{3+}$  is substituted for divalent and quadrivalent ions. These considerations are of particular importance in the first study discussed, since the calculation of the electric field gradient is very sensitive to atom positions (Bersohn, 1959).

## 5. Electron Exchange Effects

The calculations which have been discussed in the foregoing sections have been based on the assumption that the neighbours of the ion in question can be represented by point charges at the lattice points and that there is no overlap or exchange of the electrons among the ion and its neighbours. Even in "ionic" crystals this model fails to account for certain experimental observations. For example, the spin-orbit coupling constant  $\lambda$  is regularly found to be

smaller for an ion in a solid than for a free ion.

The most direct evidence that charge transfer takes place is afforded by the experiments of Tinkham (1956) on  $Mn^{++}$ ,  $Fe^{++}$ , and  $Co^{++}$  in  $ZnF_2$ . The spectra of these ions showed a "super hyperfine structure" arising from the interaction of the magnetic electrons with the surrounding fluorine nuclei.

For non-S-state ions the point charge model is generalized for electron exchange effects by adding small amounts of the ligand wave functions to the 3d wave functions, i.e. by forming linear combinations of atomic orbitals (Stevens, 1953). The reduction in the spin-orbit coupling constant  $\lambda$  is then attributed to the lower density of 3d electrons at the paramagnetic ion (Owen, 1954). To account for the observed reduction of about 25% in  $\lambda$  in this way requires that the 3d electron have 25% probability of being found on the ligand ions. Lecroix and Emch (1962) show that it may be possible to reduce the amount of covalency necessary by taking into account the charge transfer states, which involve the transfer of an electron from a bonding to an antibonding orbital. The situation is far from being resolved. Marshall and Stuart (1961) however, argue that the most important influence on  $\lambda$  comes from the screening of the 3d electrons from their parent nucleus by the overlap of the ligand electrons. This has the effect of reducing  $\lambda$  by allowing the 3d orbitals to expand ( $\lambda \sim r^{-3}$ ).

It is even more difficult to apply these methods to a reliable calculation of  $D$  because of the unknown admixture parameters involved. Rei (1962) has done a calculation based on Owen's model for  $V^{++}$  in  $T_1 O_2$ . He found that it is possible to choose plausible admixing parameters to give agreement with experimental results. Watanabe (1963) has used covalency arguments to account for the observed shifts in the  $g$  values from the free-spin value for  $S$ -state ions.

#### 6. Energy Levels of the Spin Hamiltonian for $Mn^{++}$

The energy levels of the spin Hamiltonian (2.3) are generally evaluated using perturbation methods, the last three terms being considered as perturbations on the first term. The variation of the energy levels as a function of angle between the crystal axes and the magnetic field have been evaluated by Weger and Low to the second order (Low, 1960). The calculation has been carried to the third order for the magnetic field along the three magnetic axes by Yokozawa and Kazumata (1961). Their expressions for the fine structure line positions for the magnetic field along the  $z$ -axis are:

$$H_{\pm 5/2 \leftrightarrow \pm 3/2} = H_0 \mp 4D + \frac{4E^2}{H_0} \pm 6 \frac{DE^2}{H_0^2}$$

$$H_{\pm 3/2 \leftrightarrow \pm 1/2} = H_0 \mp 2D - \frac{5E^2}{H_0} \pm 33 \frac{DE^2}{H_0^2} \quad (2.4)$$

$$H_{\pm\frac{1}{2}} \leftrightarrow -\frac{1}{2} = H_0 - \frac{8E^2}{H_0}$$

where  $H_0 = \frac{h\nu}{g\beta}$ ;  $\nu$  being the microwave frequency.

For the magnetic field parallel to the x and y-axes the line positions may be found by making the following substitutions in equations (2.4) (Bowers and Owen, 1955)

$$\begin{aligned} H//x; D \rightarrow \frac{1}{2}(3E-D), E = -\frac{1}{2}(D+E) \\ H//y; D \rightarrow -\frac{1}{2}(D+3E), E = \frac{1}{2}(D-E) \end{aligned} \quad (2.5)$$

Because of the large values of D found in the present study it was deemed advisable to test the convergence of the perturbation by carrying the calculations out to the fourth order. The details of this calculation are presented in appendix 1. The terms to be added to the equations (2.4) are

$$\begin{aligned} H_{-\frac{5}{2}} \leftrightarrow \pm \frac{3}{2} : 36 \frac{D^2 E^2}{H_0^3} + \frac{28 E^4}{H_0^4} \\ H_{-\frac{3}{2}} \leftrightarrow \pm \frac{1}{2} : 45 \frac{D^2 E^2}{H_0^3} - \frac{5 E^4}{4 H_0^3} \\ H_{+\frac{1}{2}} \leftrightarrow -\frac{1}{2} : + 72 \frac{D^2 E^2}{H_0^3} + \frac{56 E^4}{H_0^3} \end{aligned} \quad (2.6)$$

The hyperfine interaction splits each of the fine structure lines into six approximately evenly spaced lines, since the nuclear spin I of Mn is  $\frac{5}{2}$ . Since the hyperfine splitting is almost isotropic for  $Mn^{++}$ , the position of the

hyperfine lines can be described by adding

$$-A m_I - \frac{A^2}{2H_0} \left( \frac{35}{4} - m_I^2 \right) - \frac{A^2}{2H_0} (2M_s - 1) m_I \quad (2.7)$$

to each of the expressions (2.4) and (2.6) for the fine line positions, (Low, 1960). The last term in equation (2.7) permits the determination of the relative signs of D and A.

For example, for A negative the separation between the extreme hyperfine lines belonging to the  $+\frac{3}{2} \leftrightarrow +\frac{5}{2}$  fine structure line is  $\frac{20A^2}{H_0}$  greater than that for the  $-\frac{5}{2} \leftrightarrow -\frac{3}{2}$  fine structure line.

## CHAPTER III

### CRYSTALLOGRAPHY AND PHASE RELATIONSHIPS IN THE DIVALENT PHOSPHATES

The various compounds and phases of the divalent phosphates have provided a convenient series of related lattice environments for luminescent studies and should also be useful for a systematic study of changes in the axial splitting parameter  $D$  of  $Mn^{++}$ . Also, these compounds exist in a number of phases and it is possible that esr, together with x-ray, and other studies of these compounds could provide clues as to the mechanisms responsible for the transitions in these phosphates in general and in particular for the mechanisms active in the  $\alpha$  to  $\beta$  transition in  $Zn_2P_2O_7$  that is observed in this study.

There are three common types of divalent phosphates; the orthophosphate  $M_3(PO_4)_2$ , the pyrophosphate,  $M_2P_2O_7$ , and the metaphosphate,  $M(PO_3)_2$ . The phase equilibria of the zinc phosphates have been studied in some detail by Katnack and Hummel (1958). They found that there is a very sluggish reversible transition in the orthophosphate at about  $942^\circ C$ , and that the high temperature  $\beta$ -phase could be quenched as a metastable phase at room temperatures. The metaphosphate was found to undergo a sluggish irreversible phase transition

between 600 and 700°C. In contrast the zinc pyrophosphate was found to have a rapidly reversible phase transition at  $132 \pm 8^\circ\text{C}$ .

The pyrophosphate is thus the most convenient for study, both because the transition occurs at a relatively low temperature and because the rapid reversibility of the transition means that the crystals will remain stable. Similar phase transitions have been observed in the magnesium pyrophosphate at  $68 \pm 2^\circ\text{C}$  (Roy, Middlesworth and Hummel, 1948) and in  $\text{Cu}_2\text{P}_2\text{O}_7$  at  $72 \pm 2^\circ\text{C}$  (Calvo, to be published). The latter compound is not useful for esr work because the paramagnetic copper ions excessively broaden any resonance signals. This disadvantage also applies to  $\text{Mn}_2\text{P}_2\text{O}_7$ , although no transition has been found in this material. There is also another group of related divalent pyrophosphates which are of interest because of their luminescent properties when suitably activated (Ranby, Mash, and Henderson, 1955);  $\text{Ca}_2\text{P}_2\text{O}_7$ ,  $\text{Sr}_2\text{P}_2\text{O}_7$ , and  $\text{Ba}_2\text{P}_2\text{O}_7$ . These have a number of disadvantages as far as the present studies are concerned. The phase transitions which occur in these materials occur at high temperatures, above  $750^\circ\text{C}$ , and are probably irreversible (Ranby, et al, 1955). Also the Ca - O, Sr - O, and Ba - O distances are generally considerably greater than the average Mn - O distances, so that the lattice could become quite distorted near a manganese impurity, making field gradient calculations based on the host lattice structure inappropriate for the  $\text{Mn}^{++}$  ion site.

Only recently has much work been done on the crystal structures of these phosphates. The structures which have been completed are  $\gamma$ - $\text{Zn}_3(\text{PO}_4)_2$  (Calvo, 1963),  $\beta$ - $\text{Zn}_2\text{P}_2\text{O}_7$  and  $\alpha$ - $\text{Zn}_3(\text{PO}_4)_2$  (Calvo, to be published),  $\beta$ - $\text{Mg}_2\text{P}_2\text{O}_7$  and  $\beta$ - $\text{Mn}_2\text{P}_2\text{O}_7$  (Lukaszewicz and Smajkiewicz 1961). Also some preliminary work has been done on  $\alpha$ - $\text{Mg}_2\text{P}_2\text{O}_7$ ,  $\alpha$ - $\text{Zn}_2\text{P}_2\text{O}_7$  and  $\alpha$  and  $\beta$ - $\text{Cu}_2\text{P}_2\text{O}_7$  here at McMaster University.

The structure of the high temperature  $\beta$  phase of  $\text{Zn}_2\text{P}_2\text{O}_7$  is shown in figure 5. The zinc ions lie on a two-fold axis and are surrounded by six oxygens at distances of 2.18, 2.06 and 2.05 Å. Figure 6 shows the very distorted octahedron of oxygens surrounding the zinc ions down the two fold axis. The main distortion from a regular octahedron arises from the clockwise rotation of  $36^\circ$  about the two-fold axis of the two oxygen ions that lie above the plane of the figure. The pyrophosphate ion consists of corner-shared tetrahedra. The central atom of the pyrophosphate ion lies at a centre of symmetry and the mirror plane of the ion coincides with the mirror plane of the space group.

The lattice parameters and space groups of both phases of zinc pyrophosphate are listed in table 1. The notation  $3xa$  and  $2xc$  is intended to emphasize the fact that the high temperature unit cell triples along the a axis and doubles along the c axis in going to the  $\alpha$  phase and that the two structures are very closely related. The  $C - \frac{2}{m}$  space group

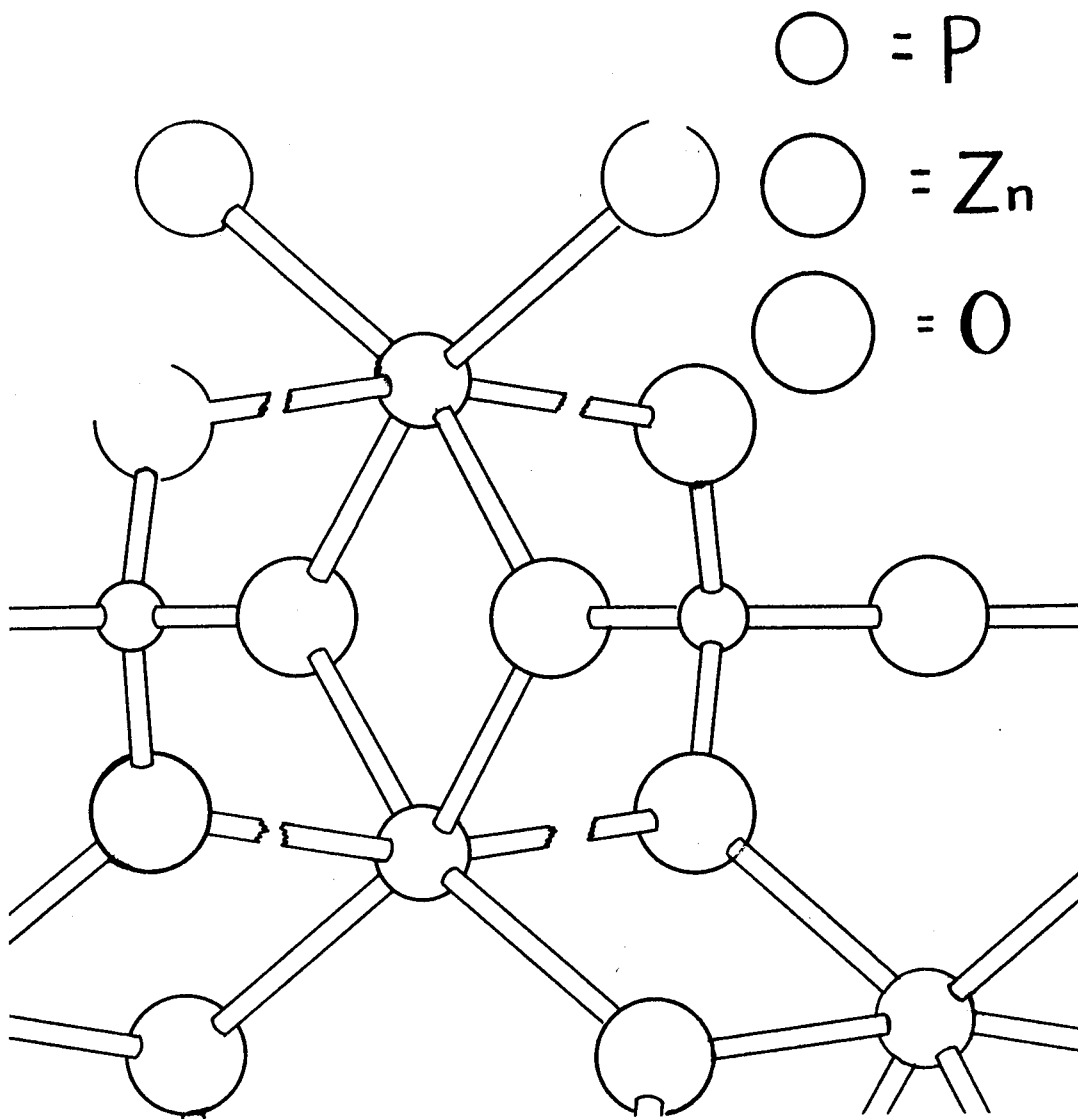


FIG. 5. THE CRYSTAL STRUCTURE OF  $\beta$ -Zn<sub>2</sub>P<sub>2</sub>O<sub>7</sub>

(International Tables for X-Ray Crystallography, Volume I, 1952) limits the number of non-equivalent cation sites to only one in  $\beta$ - $\text{Zn}_2\text{P}_2\text{O}_7$ . This can be seen by considering the equivalent positions of the space group. The four zincs are located on two-fold axes at  $0, y, \frac{1}{2}$ ;  $0, \bar{y}, \frac{1}{2}$ ;  $\frac{1}{2}, \frac{1}{2} - y, \frac{1}{2}$ ; and  $\frac{1}{2}, \frac{1}{2} + y, \frac{1}{2}$  and because of the isomorphism of  $\text{Mn}_2\text{P}_2\text{O}_7$  and  $\beta$ - $\text{Cu}_2\text{P}_2\text{O}_7$  with  $\beta$ - $\text{Zn}_2\text{P}_2\text{O}_7$  the  $\text{Mn}^{++}$  and  $\text{Cu}^{++}$  are assumed to substitute on the  $\text{Zn}^{++}$  sites. The first and third and the second and fourth positions are related to one another by translation operations (C-centering) only and thus they are equivalent. The 1st and 2nd site are related by the mirror plane and if a magnetic axis lies parallel to the two-fold axis, that is perpendicular to the mirror plane, the two sites differ only in the sense of the x and z magnetic axes. Since a magnetic axis must be parallel to the two-fold axis and esr can not distinguish an axis inversion, the two sites will appear as one. Therefore in the  $C-\frac{2}{m}$  space group with cations lying on the 2-fold axis only one site will be seen in the spectrum. The volume of the  $\alpha$ - $\text{Zn}_2\text{P}_2\text{O}_7$  unit cell space group I-C is 6 times that of the  $\beta$  form, so there are 24 cation sites per unit cell. Again the centering operation of I-C relates them in pairs and thus there may be as many as twelve non-equivalent sites in this phase.

# CATION ENVIRONMENT

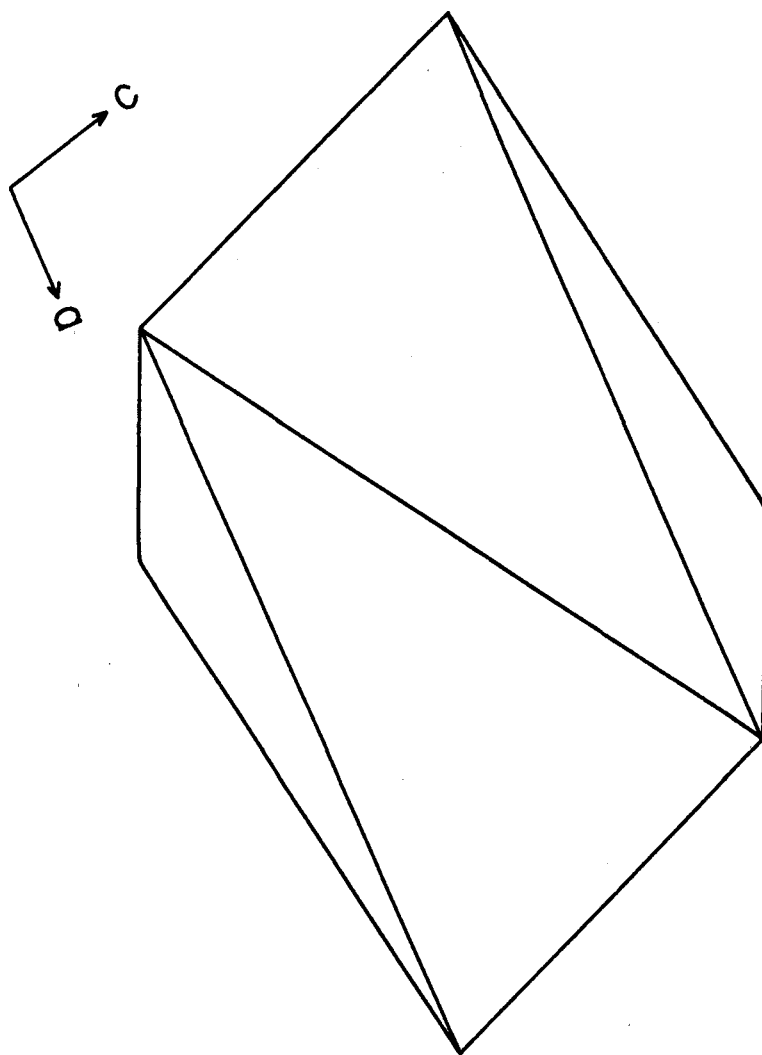


FIG.6.

Table IZn<sub>2</sub>P<sub>2</sub>O<sub>7</sub> Crystallographic Data

$\beta$ -Zn<sub>2</sub>P<sub>2</sub>O<sub>7</sub>                      Space Group C-2/m

$$a = 6.61 \text{ \AA}$$

$$b = 8.29 \text{ \AA}$$

$$c = 4.52 \text{ \AA}$$

$$\beta = 105.3^\circ$$

$\alpha$ -Zn<sub>2</sub>P<sub>2</sub>O<sub>7</sub>                      Space Group I-C

$$a = 3 \times 6.696 \text{ \AA}$$

$$b = 8.282 \text{ \AA}$$

$$c = 2 \times 4.501 \text{ \AA}$$

$$\beta = 106^\circ 16'$$

## CHAPTER IV

### EXPERIMENTAL PROCEDURE AND RESULTS

#### 1. The ESR Spectrometer

Both 3 cm. and 0.8 cm. esr spectrometers were used in this study. A block diagram of the 3 cm. spectrometer is shown in figure 7 (Pieczonka, 1960). The 3 cm. wavelength microwave energy is generated by the klystron and propagated down a rectangular waveguide through a uniline, a frequency meter and a variable attenuation to arm 1 of the magic tee. The magic tee has the property that when arms 4 and 2 are terminated in equal impedances no power is transmitted into arm 3. The absorption of power by the sample in the microwave cavity in arm 4 upsets this balance and a signal is detected in arm 3. The absorption signal is modulated by the modulation of the d.c. magnetic field by the coils shown on the magnet pole pieces. The modulated absorption signal is then amplified and detected in a phase sensitive detector. The d.c. output of the phase sensitive detector is then fed to a chart recorder. Also shown in figure 7 is a frequency control loop which locks the klystron frequency to the resonant frequency of the microwave cavity. The construction and operation of the 0.8 cm. spectrometer<sup>1</sup> is quite similar

---

1

This spectrometer was provided by Professor W.R. Daters of the Physics Department at McMaster University.

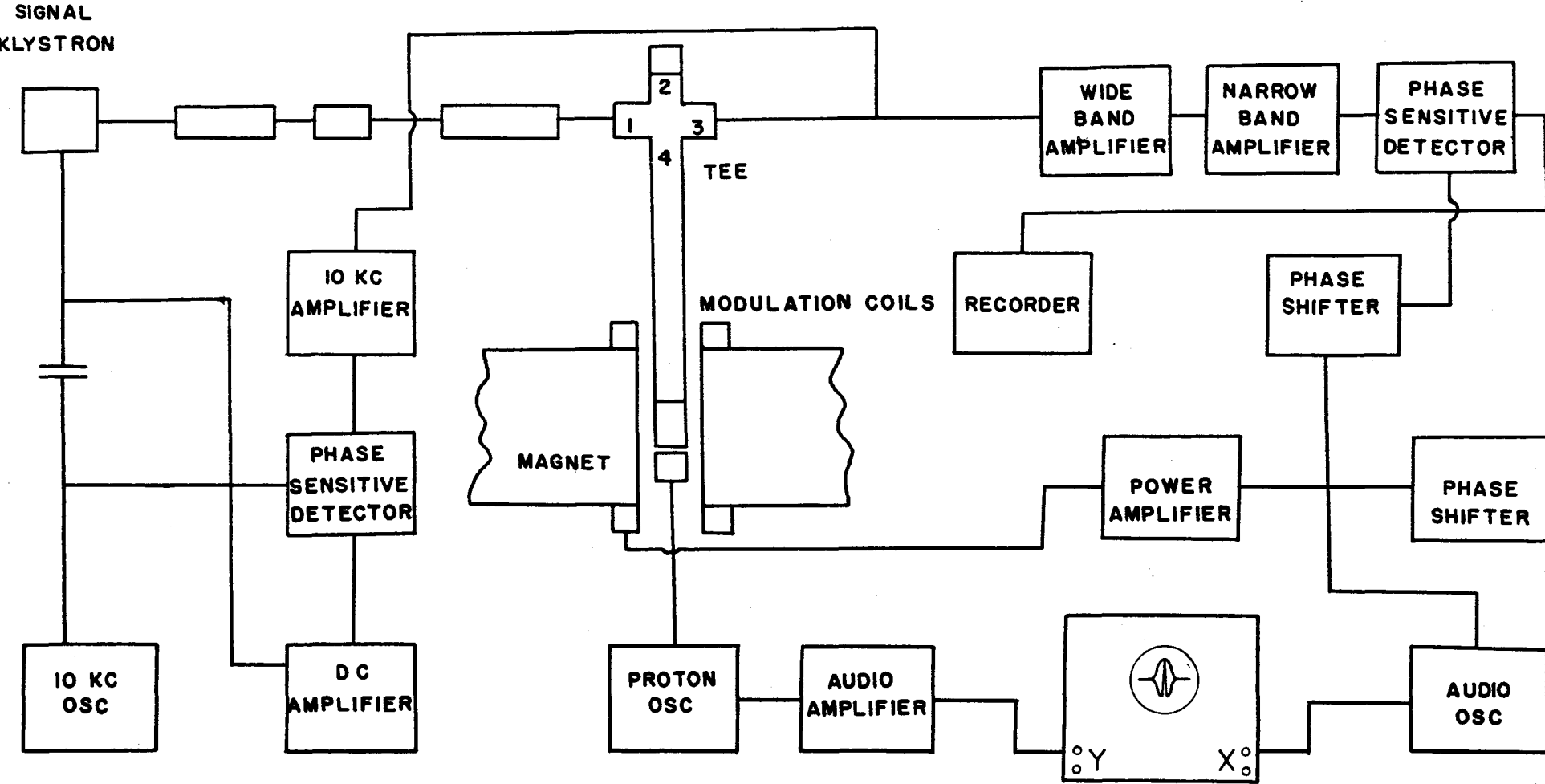


FIG. 7. BLOCK DIAGRAM OF THE 3 CM. ESR SPECTROMETER

to that of the 3 cm. spectrometer.

A Varian 6 inch magnet was used, with a  $1\frac{1}{2}$  inch gap for the 3 cm. experiments and a  $\frac{1}{2}$  inch gap for the 0.8 cm. experiments. The power supply and magnetic field drive mechanism are described by Pieczonka (1957).

## 2. The 3 cm. Sample Holder and Oven

Because of the low unit cell symmetry of  $\alpha$ - $\text{Zn}_2\text{P}_2\text{O}_7$  it was necessary to be able to rotate the sample about two perpendicular axes in order to determine the direction of the magnetic axes experimentally.

The design of the sample holder is illustrated in figure 8. The large outer shaft allows rotation about an axis which is set perpendicular to the magnetic field. The non-concentric inner shaft rotates the sample about an axis perpendicular to the first axis, by means of the right angled gear system shown.

The sample holder had to be made of a relatively low - loss - dielectric material which would not excessively lower the Q of the microwave cavity, and yet be able to withstand temperatures up to about 200°C without change of its mechanical properties. The gears and the part of the sample holder that entered the oven were cast from Stycast 2651, supplied by Emerson and Cumming Inc. It was found that the Stycast part of the center shaft tended to distort under the gear pressure at high temperatures, so that this part was

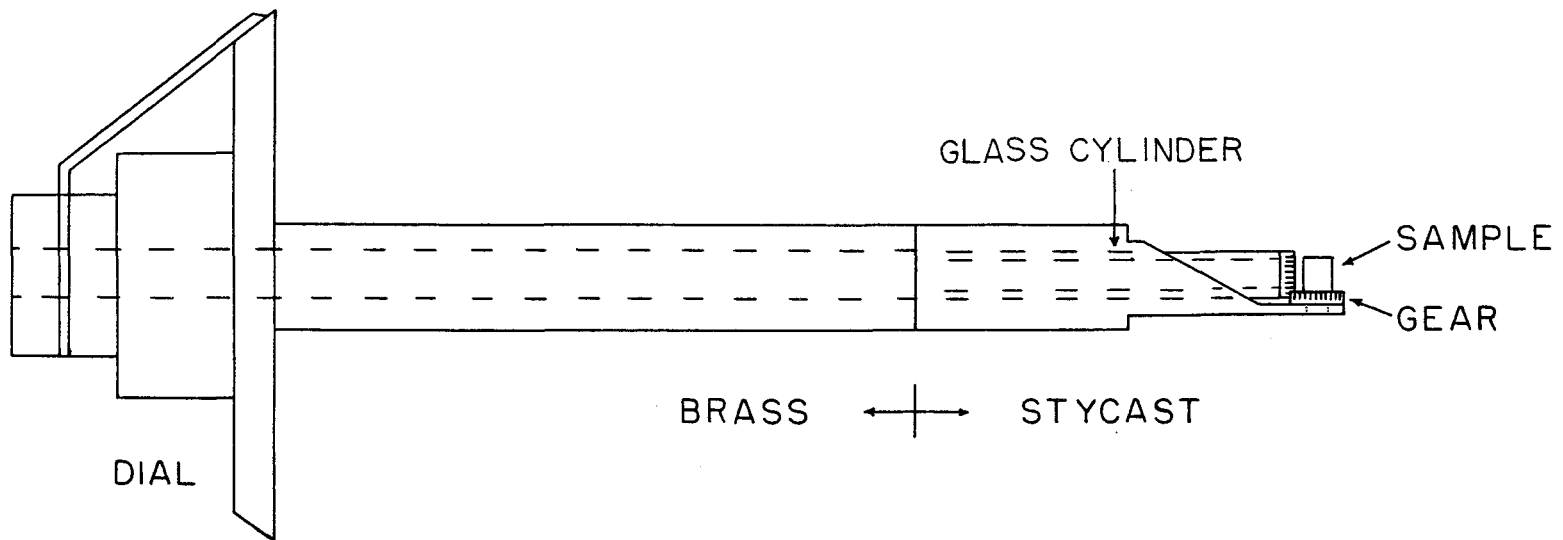


FIG. 8. THE 3 CM. SAMPLE HOLDER DESIGN

strengthened by a glass rod, as shown in figure 9. The gears were cast in moulds made from modeling clay. The  $\frac{1}{4}$ " brass mitre gears, supplied by the Boston Gear Co. and cut down to  $\frac{1}{4}$ " outside diameter, were used to form the moulds. Using optical methods it was found that the setting of the sample holder was reproducible to  $\pm \frac{1}{2}^\circ$ , limited by the gear backlash. The glass rod cracked on cooling but still remained serviceable.

The sample holder shown in figure 8 is supported by a brass support shown in figure 9. This support was designed to clamp between the magnet coil supports. The oven is made of Supramica, supplied by the Mycalex Corp. of America, and was designed to slip over the microwave cavity assembly. The heating element is about 5 feet of number 27 nichrome wire wound on a ceramic core. The overall width of the oven is  $1\frac{1}{8}$  inches. About 45 watts of input electrical power are required to reach a temperature of  $200^\circ\text{C}$ .

### 3. The 0.8 cm. Sample Holder and Oven

The small size of the 0.8 cm. microwave cavity made it impracticable to provide facilities for rotation about two axes. The sample is mounted on the end of a  $\frac{5}{32}$ " diameter ceramic rod as shown in figure 10. A thermocouple is mounted as shown, in contact with the crystal. The crystal is affixed to the end of the rod with Stycast 2651, which covers both crystal and thermocouple and ensures good thermal contact.

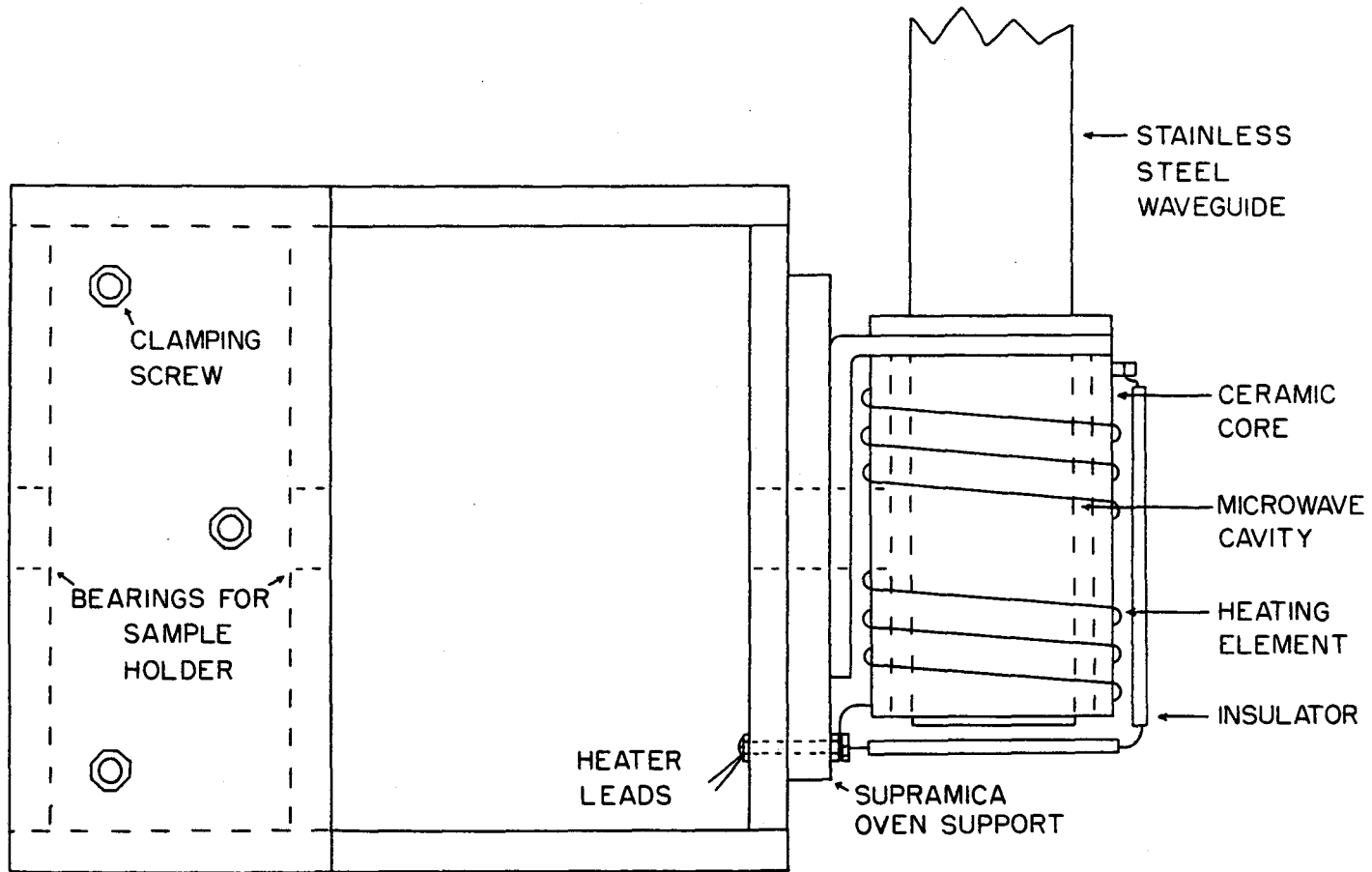


FIG. 9. THE 3 CM. MICROWAVE CAVITY AND OVEN ASSEMBLY

The sample holder is supported by a frame which is clamped to a piece of 3 cm. waveguide such that the axis of rotation of the sample is parallel to the waveguide. The microwave cavity and oven assembly is also clamped to this waveguide so as to position the sample properly in the cavity. The assembled unit is shown schematically in figure 10. The waveguide fits snugly between the magnet pole-pieces when they have the  $\frac{1}{2}$  inch gap necessary to obtain the high fields required for 0.80 cm. operation. Thus the axis of rotation is aligned parallel to the pole faces. The oven is made of Supramica in a manner similar to the 3 cm. oven, except that the total overall thickness is now  $\frac{7}{16}$  inch. Because the thinner walls allow greater heat losses, about 75 watts of input power are necessary to reach a temperature of 200°C.

The power supply for both ovens was a full-wave selenium rectifier bridge with a rated output of 5 amperes at 90 volts. To obtain sufficiently fine temperature control this power supply was controlled by two Variacs in series. Since fluctuations of the line voltage caused temperature variations in the ovens of as much as 7°C it was necessary to use a constant voltage transformer. It was then found that fluctuations over a period of hours were not greater than  $\pm 0.5^\circ\text{C}$ . The temperature of the sample was monitored during the experiment with a Phillips millivolt recorder and measured with a Pye Type P4 thermocouple potentiometer.

The accuracy with which the temperature of the sample

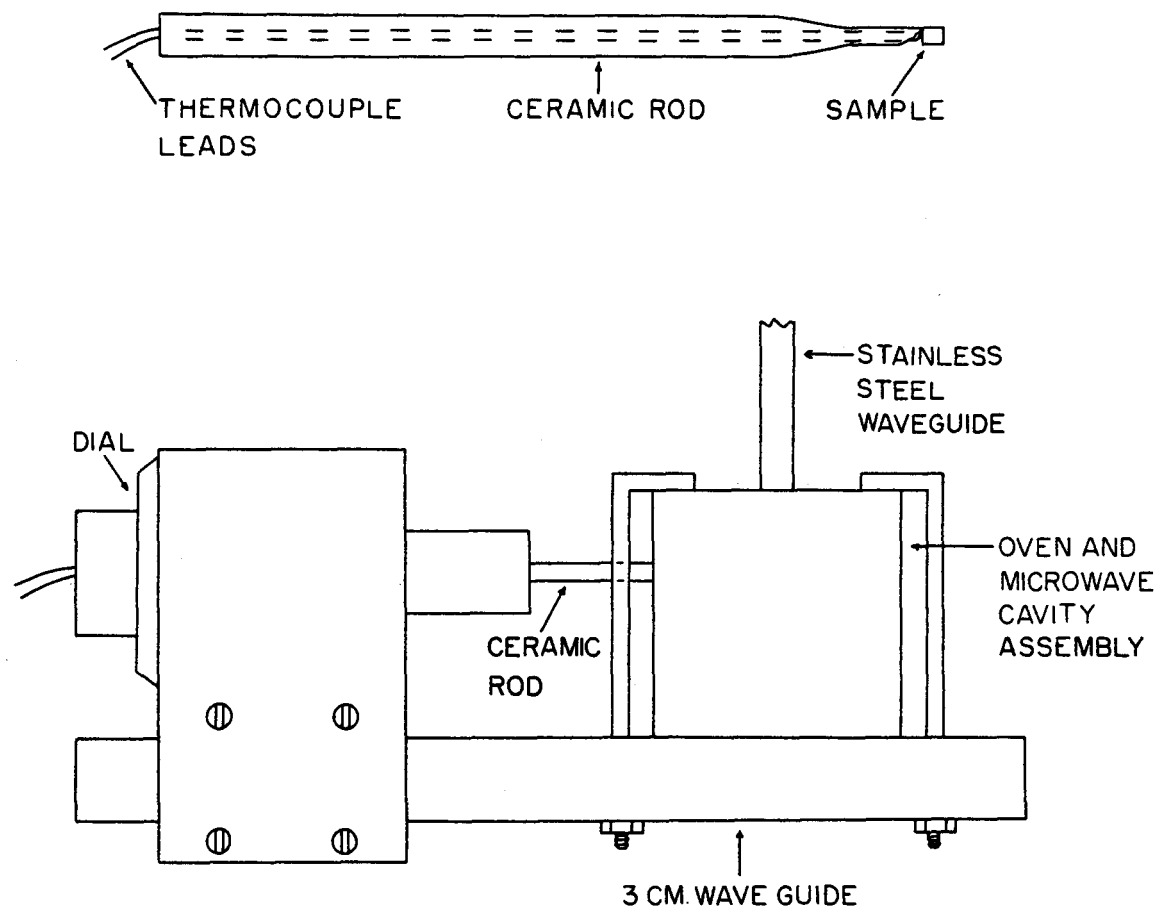


FIG. 10. THE 0.8 CM. SAMPLE HOLDER AND OVEN ASSEMBLY

could be measured was limited by an effect which was difficult to evaluate precisely. As the sample was rotated in the oven it was noted that the measured temperature varied by as much as  $5^{\circ}$ . Since the heating element in the 0.8 cm. oven is situated just below the opening for the sample holder it is assumed that this change in temperature results from the difference in thermal conductivity between the Stycast and the ceramic rod. When the ends of the ceramic rods were ground down to permit them to enter the cavity, as shown in figure 10, the two holes for the thermocouple wire become exposed and often the end of the rod chips in an unsymmetrical fashion. These openings are all filled in with Stycast when the sample is mounted. It was found that the temperature was highest when the Stycast portions are nearest the heating elements. Although there is undoubtedly a temperature gradient set up along the ceramic rod in this region it is likely that the major part of the observed variation represents a real change in the crystal temperature, since the thermocouple is next to the sample and is kept in thermal contact with it by the Stycast. Because of these considerations and because the lower transition temperature was consistently found to be near  $132^{\circ}\text{C}$  a maximum uncertainty of  $\pm 2^{\circ}\text{C}$  is assigned to the temperature measurements for the 0.8 cm. data.

#### 4. Alignment of the Sample

The symmetry of the crystal lattice is reflected in

the spin Hamiltonian, so that the two-fold axis which exists in  $\beta\text{-Zn}_2\text{P}_2\text{O}_7$  is also one of the paramagnetic axes. Since the three susceptibility axes are orthogonal, the remaining two axes lie in the plane perpendicular to the two-fold axis. For at constant microwave frequency, the magnetic field at which resonance occurs for a given transition passes through either a minimum or a maximum when a susceptibility axis is parallel to the magnetic field. Thus the esr spectrum can be used to locate these axes. This task is simplified in the case of  $\beta\text{-Zn}_2\text{P}_2\text{O}_7$  since the existence of the two-fold axis fixes one of the magnetic axes and confines the other two to a plane perpendicular to it.

The samples<sup>1</sup> were first aligned on a regular x-ray goniometer head, using either an oscillation or precession camera. Each sample to be studied with the 0.8 cm. spectrometer was then glued to a ceramic rod with the two-fold axis either perpendicular or parallel to the axis of the rod. Two devices were constructed to accomplish these orientations. One was merely a large brass cylinder which would slide into the film holder of the Weissenberg camera with the ceramic rod projecting from a hole in the center. The other was a small brass adapter which holds the ceramic rod in the position of the x-ray beam in the precession camera.

---

<sup>1</sup>Single crystals were grown from the melt. The  $\text{Zn}_2\text{P}_2\text{O}_7$  was prepared as described by Rieman, Neuss, and Naiman (1942).

After a sample had been glued to the rod with Stycast, the alignment was checked to ensure that the crystal had not moved during the glueing. To do this, an adapter was made which when attached to a regular goniometer head base allowed oscillation or Weissenberg photographs of the sample to be taken. The alignment remained true to an accuracy of  $\pm 1^\circ$ .

Each sample for use with the 3 cm. spectrometer was glued to the appropriate gear (figure 8) in roughly the desired orientation and final adjustments were made by using the esr spectra to align the paramagnetic axes parallel to the magnetic field. This adjustment was carried out to an accuracy of  $\pm 2^\circ$  for both the 3 cm. and 0.8 cm. samples.

#### 5. Spectra of $\text{Cu}^{++}$ and $\text{Mn}^{++}$ at Various Temperatures

In this section the general behaviour of the spectra obtained will be discussed. As anticipated in Section (II, 1) the  $\text{Cu}^{++}$  spectrum consists of four lines with hyperfine interval A. Figure 11 shows the spectra of  $\text{Cu}^{++}$  at various temperatures with the  $z$ -axis parallel to the magnetic field. The quantity plotted on the abscissa is the first derivative of the energy absorbed by the spin system. The klystron frequency was held constant and the magnetic field is plotted along the ordinate axis. It can be seen that the high temperature lines have begun to split when the sample is cooled to  $150^\circ\text{C}$ . This splitting increases down to  $132.5^\circ\pm 0.5^\circ\text{C}$ . At this temperature it changes abruptly to the spectrum shown at  $132^\circ\text{C}$  and the line positions remain essentially

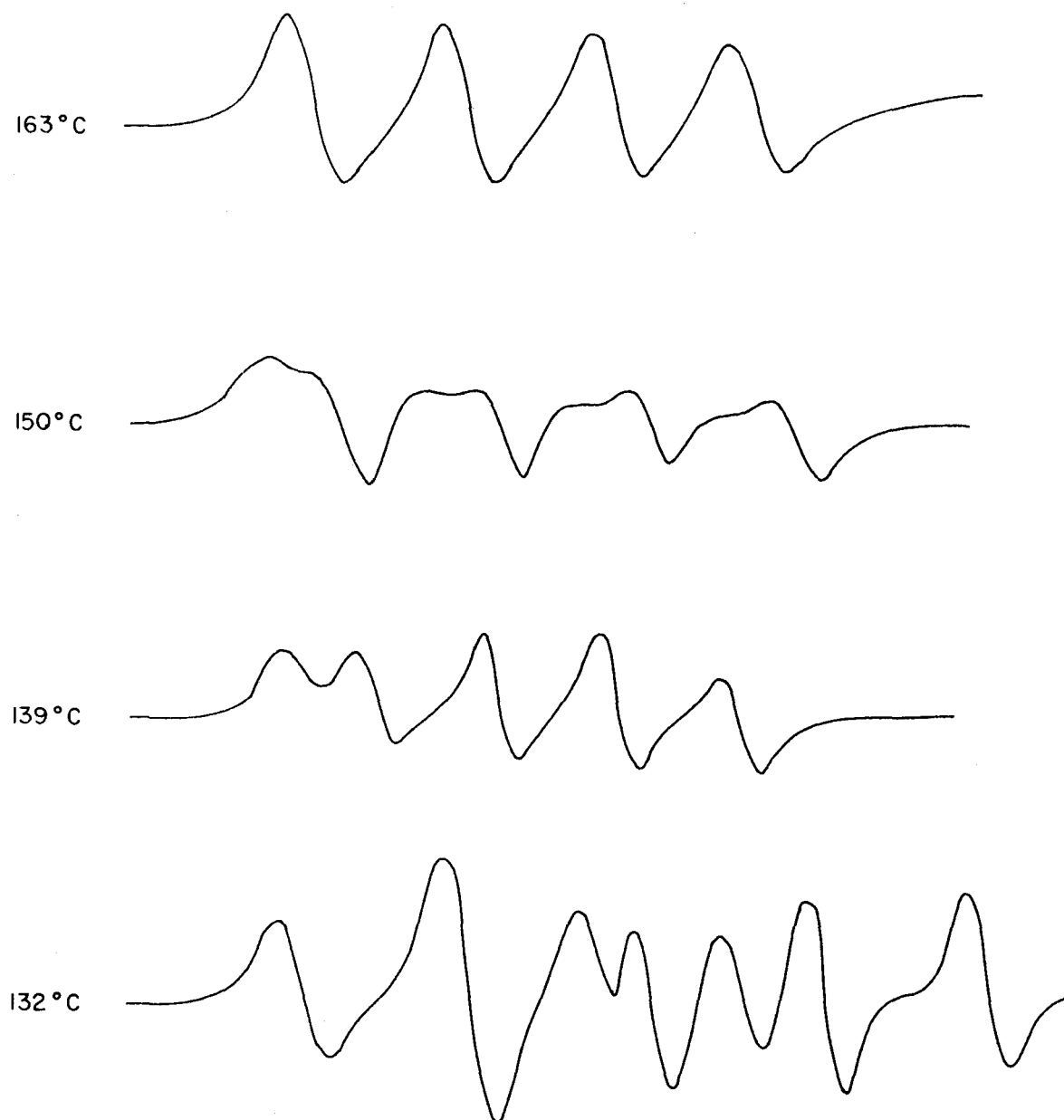


FIG. II. ESR SPECTRA OF  $\text{Cu}^{2+}$  IN  $\text{Zn}_2\text{P}_2\text{O}_7$ , WITH H//Z -AXIS AT VARIOUS TEMPERATURES

unchanged down to room temperature.

The spectra with the x & y-axes parallel to the magnetic field are not so informative. Figure 12 shows these spectra for various temperatures. The value of A along these axes is so small that only a single line with a peak to peak line width of about 50 gauss is obtained, at intermediate temperatures the y axis line becomes somewhat asymmetric, but does not detectably split. The origin of the two low intensity lines which are present in the x-axis spectrum in the intermediate and low temperature ranges is not understood.

The high temperature  $Mn^{++}$  spectra consists of five groups of six lines. The overall splitting of each group is approximately 450 gauss and the interval between the centers of the groups varies between 850 and 2200 gauss when the magnetic field is parallel to a magnetic axis. Because of the limitations of the magnet used it was only possible to record three or four of the lower field groups. The second lowest of these lines, corresponding to the  $+ \frac{3}{2} \leftrightarrow + \frac{1}{2}$  fine structure line is shown in figure 13 for various temperatures with the y-axis of the  $\beta-Zn_2P_2O_7$  (the two-fold axis) parallel to the magnetic field. The lines broaden as the upper transition at about  $155^\circ C$  is approached from above. The six lines at  $183^\circ C$  are just barely discernible at  $164^\circ C$ . At  $155^\circ C$  the splitting has just begun. Although it is not possible to pick out all of the lines of the two sites, the

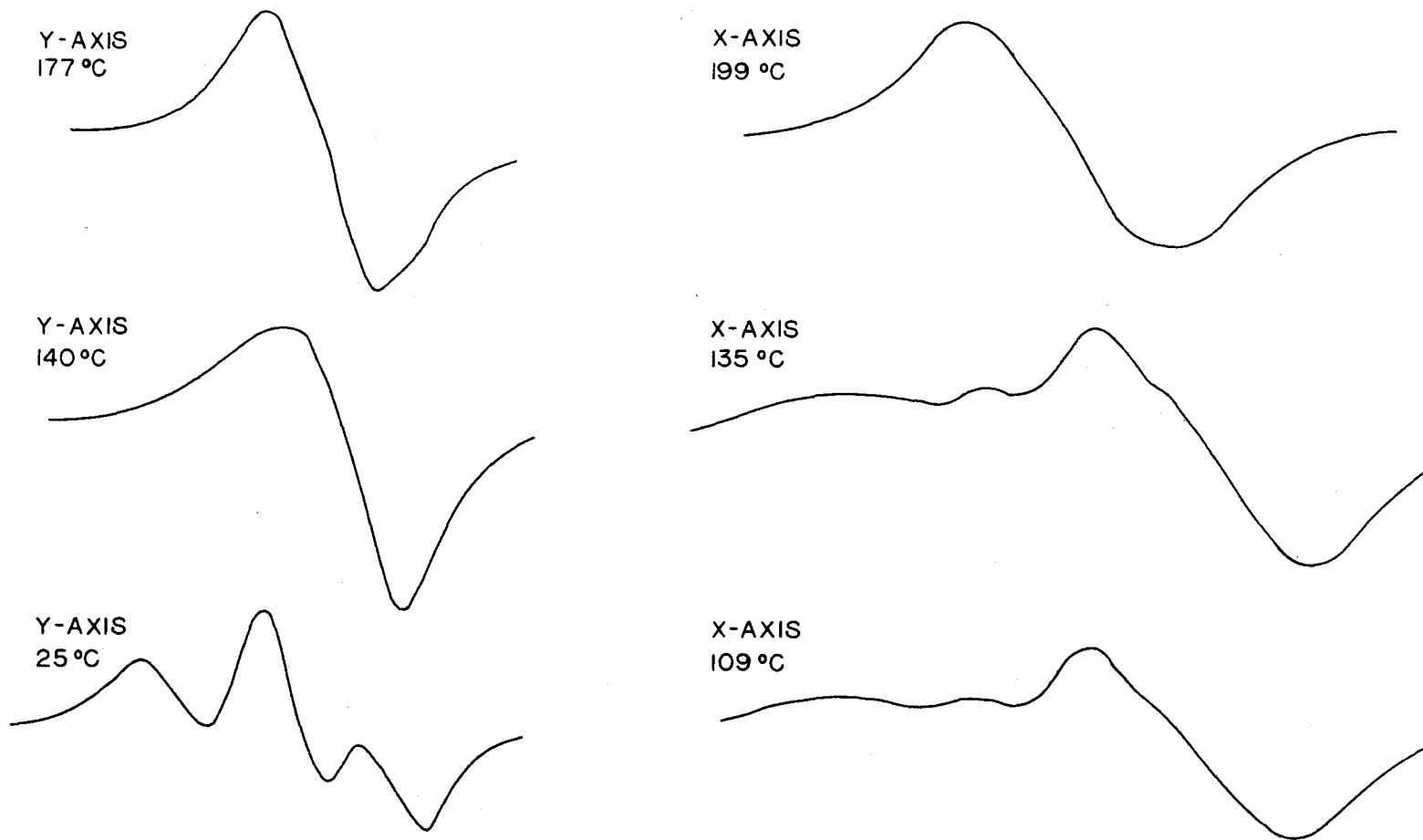


FIG. 12. ESR SPECTRA OF  $\text{Cu}^{2+}$  IN  $\text{Zn}_2\text{P}_2\text{O}_7$ , WITH  $\text{H} // \text{X}$  AND  $\text{H} // \text{Y}$  AT VARIOUS TEMPERATURES

first two peaks at low magnetic field are separated from the last two at the high field end of the spectrum by the same interval as the two extreme peaks at  $164^{\circ}\text{C}$  and are separated from one another by  $44 \pm 10$  gauss.

The lower set of lines at  $147^{\circ}\text{C}$  are not as intense as the upper set. The two lowest line positions are indicated by arrows. The much broadened high temperature line is still in evidence even at  $135^{\circ}\text{C}$ , just above the lower transition. The behaviour illustrated in figure 13 is typical of the spectra for all three magnetic axes.

#### 6. Angular Variations of the Magnetic Axes

It should be noted here that the spectra between  $132^{\circ}\text{C}$  and  $155^{\circ}\text{C}$  are measured parallel to the high temperature magnetic axes. It was found experimentally that at about  $134^{\circ}\text{C}$  the magnetic axes had shifted by as much as  $4^{\circ}$ . Because of the orientational difficulties mentioned above it is not possible to tell precisely what directional changes take place in the magnetic axes. The goodness of fit of the spectra to the expressions for the line positions (2.4) and (2.6) is a fairly sensitive indication of the deviation of the  $z$ -axis from its high temperature position, but because of the small value that is found for  $E$  the line positions are relatively insensitive to rotations of the other two axes about the  $z$ -axis. This point will be elaborated upon below.

Although the line positions of the  $\text{Cu}^{++}$  spectra do

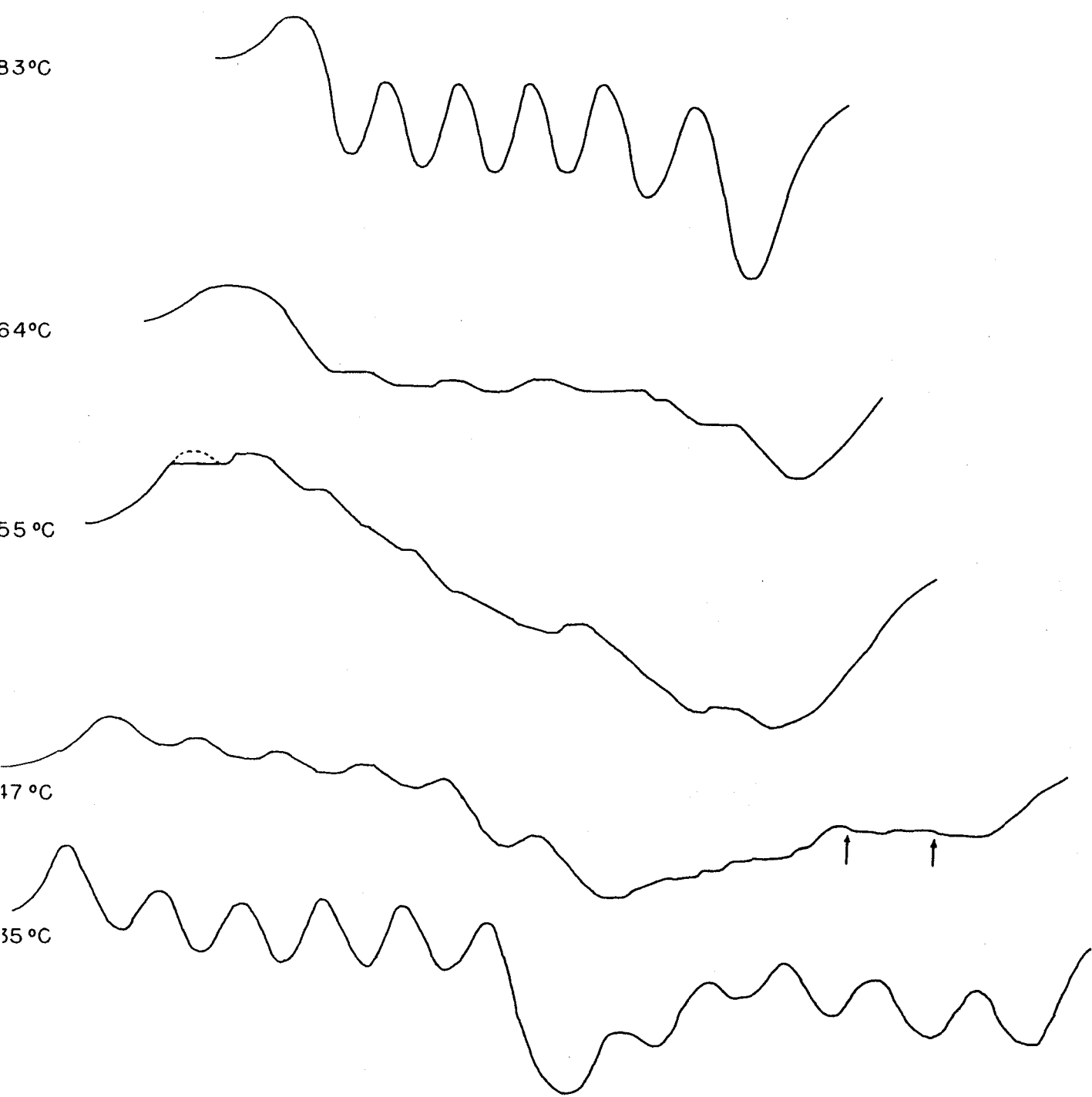


FIG. 13. ESR SPECTRA OF Mn<sup>2+</sup> IN Zn<sub>2</sub>P<sub>2</sub>O<sub>7</sub>, WITH H//Y AT VARIOUS TEMPERATURES

not shift much on going from 132.5°C to room temperature the relative amplitudes of the derivative curves do. The  $Mn^{++}$  spectra behave in a similiar fashion, although the interpretation is not as straight forward because of their greater complexity. There is an abrupt change at about 132°C, but intensity changes continue at least down to 100°C. Since the intensities of the  $Mn^{++}$  spectra lines change as the magnetic axes move away from being parallel to the magnetic field it is difficult to distinguish changes in intensity due to possible population differences of the various cation sites in the lattice from these angular variations. To be able to sort out these effects in this region would require being able to follow the magnetic axes as they move. These angular changes do not all take place abruptly at the lower transition. For example, at room temperature evidence for at least three different sites was found. Although the direction of the magnetic axes of these sites was not established, measurements along three axes near the high temperature axes were made for one of these sites. One of the other low temperature sites is very similar to the one measured, with the  $\pm 3/2 \leftrightarrow \pm 1/2$  lines nearly coinciding along the x-axis. At 128°C with the magnetic field parallel to the x-axis of the  $\beta-Zn_2P_2O_7$  these two sets of lines are less than 6 gauss apart. At 122°C they are about 18 gauss apart and at room temperature about 38 gauss apart. Thus, some changes are still taking place

considerably below 132°C.

The actual direction for the low temperature y-axis measurements was chosen about 4° away from the high temperature y-axis because it was only there that it was possible to resolve the six lines of a particular site. The x and  $\zeta$ -axes measurements were made at directions rotated 9° about the high temperature 2-fold axis from the high temperature x and  $\zeta$ - axes positions. At this position the two low temperature sites mentioned above were separated by only about 14 gauss. Even though these room temperature measurements were not made with the magnetic axes properly aligned it will be shown later that they give reasonably accurate values for the spin Hamiltonian parameters.

## 7. Measurement of the Line Positions

The magnetic field calibration was made by measuring the nuclear magnetic resonance frequency of either proton (at 3 cm.) or lithium nuclei (0.8 cm.) magnetic moments situated near the resonant cavity. Actually the cavity and the nuclear resonance sample were placed 1 inch on either side of centre of the magnet pole pieces. The nuclear resonance signal was displayed on an oscilloscope screen and as this signal crossed the center of the screen a marker was drawn on the chart paper by shorting the input terminals of the recorder temporarily. The frequency of the proton oscillating detector was then measured with a Bendix Radio

BC-221-M beat frequency oscillator. The magnetic field was swept at a rate varying from about 30 to 50 gauss per minute. The modulation of the nuclear resonance signal was supplied by the esr modulation coils and was about 20 gauss peak-to-peak. The magnetic field could be measured to an accuracy of  $\pm 1$  gauss in this manner, but other factors increased the error in the measured line positions to the values shown in the tables of data.

The rectified signal from the phase sensitive detector in figure 7 passes through an RC filter before going to the recorder. Increasing the time constant of this filter improves the sensitivity of the detection system but will eventually distort the signal. A reasonable compromise between improved sensitivity and error in line position due to this distortion was achieved with a time constant of 8 seconds. The amount of distortion was determined by sweeping the magnetic field through the resonance signals in both directions, and taking the average line position. This procedure contributes an uncertainty in line position of between  $\pm 0.5$  to  $\pm 1$  gauss depending on the signal amplitude.

The magnetic field drive speed fluctuated somewhat, chiefly because of worn or dirty potentiometers in the drive circuit. This could be seen as a slight irregularity in the progress of the nuclear resonance signal across the oscilloscope screen and in nonlinear magnetic field intervals on the chart paper. This effect was minimized by putting

calibration markers near the line positions.

The effect of this and other random errors could be seen in the departure of the hyperfine intervals from the values predicted by equation (2.7). The line positions obtained for  $Mn^{++}$  with the 0.8 cm. spectrometer are given in column 5 of table 2. The first column denotes the axis parallel to the magnetic field when the measurement was taken, the second the temperature of the sample, the third the electronic transition and the fourth the nuclear quantum number. The sixth column gives the average values of the two central hyperfine transitions. The errors quoted for these average values are the sums of the random errors needed to encompass the irregularities in the hyperfine structure and the errors due to the distortions of the signals described above. There are some cases where one line position in a hyperfine group is obviously wrong, either because of overlapping lines or a poor reading. In these instances this line position corrected to give the proper hyperfine intervals is used in computing the average value in column 6. The  $Cu^{++}$  data are presented in table 3. The errors quoted for the data taken about the x and y-axes are based on an alignment accuracy in the magnetic field of  $\pm 1^\circ$  and are considerably larger than the contributions discussed above. The errors for the  $z$ -axis spectra are obtained in the manner described above for the  $Mn^{++}$  spectra.

The line positions marked "Std." in table 2 or with an asterick in table 3 are the signals from the charred charcoal

samples which are glued to the crystals under study. These samples are prepared by charring sugar and mixing it with a Stycast fixer. It has been found (Ingram, 1954) that the spectroscopic splitting factor of  $g = 2.0030 \pm 0.0003$  obtained for these chars is constant up to about  $600^\circ\text{C}$ . The errors for these lines are  $\pm 1.5$  gauss for the high temperature lines and  $\pm 2$  gauss for the remaining lines. The errors quoted for the  $g$ -values in the tables 4 and 6 are just the random errors and do not include a possible systematic error in the above  $g$ -value. The line positions denoted by "u" are either unresolved or unmeasured.

#### 8. Determination of the Spin Hamiltonian Parameters for $\text{Mn}^{++}$

The absolute values of the spin Hamiltonian parameters for  $\text{Mn}^{++}$  can be obtained by fitting equations (2.4) and (2.6) to the fine structure line positions. These line positions can be obtained from the  $H_{av}$  values in Table 2 by adding to them a correction arising from the second order hyperfine effects indicated in equation (2.7). This correction is  $17A^2/4H_0 = 2.8$  gauss for  $A = 90$  gauss and  $H_0 = 1.2 \times 10^4$  gauss. The procedure for determining these parameters is simplified if the rhombic splitting parameter  $E$  is small. Consider the high temperature spectra as an example. If  $E$  is less than about 70 gauss the interval between the  $-3/2 \rightarrow -1/2$  and the  $-1/2 \rightarrow +1/2$  fine structure

TABLE IIPosition of esr Lines in Gauss in Mn:  $Zn_2P_2O_7$ 

Axis	Temp. ( $^{\circ}C$ )	Transition	m	Line Position	$H_{av}$
z	175	$-3/2 \rightarrow -1/2$	-5/2	9759	$9977 \pm 3$
			-3/2	9846	
			-1/2	9932	
			+1/2	10021	
			+3/2	10117	
			+5/2	10213	
z	175	$-1/2 \rightarrow +1/2$	-5/2	11957	$12184 \pm 2$
			-3/2	12048	
			-1/2	12138	
			Std.	12173	
			+1/2	12230	
			+5/2	12413	
x	184	$+1/2 \rightarrow -1/2$	-5/2	11762	$11984 \pm 2$
			-3/2	11852	
			-1/2	11939	
			+1/2	12028	
			+3/2	12118	
			Std.	12173	
x	186	$+3/2 \rightarrow +1/2$	-5/2	10738	$10962 \pm 3$
			-3/2	10829	
			-1/2	10919	
			+1/2	11006	
			+3/2	11096	
			+5/2	11190	
x	185	$-1/2 \rightarrow -3/2$	-5/2	12940	$13161 \pm 4$
			-3/2	u	
			-1/2	13117	
			+1/2	13205	
			+3/2	u	
			+5/2	u	
x	186	$+5/2 \rightarrow +3/2$	-5/2	9793	$10020 \pm 3$
			-3/2	9887	
			-1/2	9967	
			+1/2	10062	
			+3/2	10157	
			+5/2	10250	

TABLE II (Continued)

Axis	Temp. (°C)	Transition	m	Line Position	How
y	183	$+1/2 \rightarrow -1/2$	-5/2	11697	11907 $\pm$ 2
			-3/2	11787	
			-1/2	11874	
			+1/2	11961	
			+3/2	12049	
			+5/2	u	
y	183	$+5/2 \rightarrow +3/2$	std.	12101	10063 $\pm$ 3
			-5/2	9841	
			-3/2	9929	
			-1/2	10022	
			+1/2	10107	
			+3/2	10198	
y	183	$+3/2 \rightarrow +1/2$	+5/2	10291	10933 $\pm$ 3
			-5/2	10716	
			-3/2	10803	
			-1/2	10889	
			+1/2	10978	
			+3/2	11070	
y	183	$-3/2 \rightarrow -1/2$	+5/2	11162	13040 $\pm$ 3
			-5/2	12823	
			-3/2	12909	
			-1/2	12996	
			+1/2	13084	
			+3/2		
z	136	$-1/2 \rightarrow +1/2$	+5/2		12193 $\pm$ 3
			-5/2	11969	
			-3/2	12057	
			-1/2	12148	
			std.	12183	
			+1/2	u	
z	136	$-3/2 \rightarrow -1/2$ (Upper Set)	+3/2	u	10419 $\pm$ 5
			+5/2	u	
			-5/2	u	
			-3/2	10288	
			-1/2	10374	
			+1/2	10464	
+3/2	10561				
+5/2	10644				

TABLE II (Continued)

Axis	Temp. (°C)	Transition	m	Line Position	$H_{av}$
z	136	-3/2 → -1/2 (Lower Set)	-5/2	9346	9555 <sup>±7</sup>
			-3/2	9422	
			-1/2	9512	
			+1/2	9597	
			+3/2	9683	
			+5/2	u	
x	137	+1/2 → -1/2 (Upper Set)	-5/2	11831	12056 <sup>±4</sup>
			-3/2	11921	
			-1/2	12018	
			+1/2	12101	
			Std.	12185	
			+3/2	u	
x	137	+1/2 → -1/2 (Lower Set)	-5/2	11706	11921 <sup>±4</sup>
			-3/2	11790	
			-1/2	11877	
			+1/2	11967	
			+3/2	12055	
			+5/2	u	
x	137	+3/2 → +1/2 (Upper Set)	-5/2	10990	11215 <sup>±4</sup>
			-3/2	11079	
			-1/2	11168	
			+1/2	11261	
			+3/2	11353	
			+5/2	11444	
x	137	+3/2 → +1/2 (Lower Set)	-5/2	10528	10740 <sup>±4</sup>
			-3/2	10612	
			-1/2	10696	
			+1/2	10783	
			+3/2	10869	
			+5/2	u	
y	133	+1/2 → -1/2 (Upper Set)	-5/2	11831	12060 <sup>±4</sup>
			-3/2	11921	
			-1/2	12014	
			+1/2	12106	
			Std.	12188	
			+3/2	u	
		+5/2	12284		

TABLE II (Continued)

Axis	Temp. (°C)	Transition	m	Line Position	$H_{av}$
y	133	+1/2 → -1/2 (Lower Set)	-5/2	11701	11930 <sup>±</sup> 8
			-3/2	11781	
			-1/2	u	
			+1/2	u	
			+3/2	u	
			+5/2	u	
		Std.	12188		
y	135	+3/2 → +1/2 (Upper Set)	-5/2	u	11261 <sup>±</sup> 5
			-3/2	11125	
			-1/2	11215	
			+1/2	11306	
			+3/2	11398	
			+5/2	11494	
y	135	+3/2 → +1/2 (Lower Set)	-5/2	10558	10777 <sup>±</sup> 5
			-3/2	10647	
			-1/2	10733	
			+1/2	10821	
			+3/2	10904	
			+5/2	u	
z	Room	-1/2 → +1/2	-5/2	11972	12209 <sup>±</sup> 2
			-3/2	12066	
			-1/2	12162	
			Std.	12205	
			+1/2	12255	
			-3/2	12244	
		-5/2	12437		
z	Room	-3/2 → -1/2	-5/2	10754	10984 <sup>±</sup> 2
			-3/2	10845	
			-1/2	10938	
			+1/2	11030	
			+3/2	11123	
			+5/2	11216	
z	Room	+1/2 → +3/2	-5/2	12996	13432 <sup>±</sup> 5
			-3/2	13201	
			-1/2	u	
			+1/2	u	
			+3/2	u	
			+5/2	u	

TABLE II (Continued)

Axis	Temp. (°C)	Transition	m	Line Position	$H_{av}$
x	Room	+1/2→-1/2	-5/2	11939	12167±3
			-3/2	12033	
			-1/2	12121	
			Std.	12201	
			+1/2	u	
			+3/2	12311	
			+5/2	12407	
x	Room	+3/2→+1/2	-5/2	11300	11530±5
			-3/2	11390	
			-1/2	11479	
			+1/2	11578	
			+3/2	11669	
			+5/2	11756	
x	Room	-1/2→-3/2	-5/2	12308	12831±5
			-3/2	12696	
			-1/2	12785	
			+1/2	12877	
			+3/2	12965	
			+5/2	13063	
y	Room	+1/2→-1/2	-5/2	11932	12159±4
			-3/2	12021	
			-1/2	12113	
			Std.	12194	
			+1/2	u	
			+3/2	12305	
			+5/2	12404	
y	Room	+3/2→+1/2	-5/2	11422	11655±5
			-3/2	11511	
			-1/2	11608	
			+1/2	11694	
			+3/2	11791	
			+5/2	u	
y	Room	-1/2→-3/2	-5/2	u	12692±5
			-3/2	12552	
			-1/2	12646	
			+1/2	12737	
			+3/2	12829	
			+5/2	12916	

TABLE II (Continued)

Axis	Temp. (°C)	Transition	m	Line Position	Har
z	144	$-1/2 \rightarrow +1/2$	-5/2	11967	12193 <sup>±3</sup>
			-3/2	12054	
			-1/2	12148	
			Std.	12180	
			+1/2	12237	
			+3/2	12328	
			+5/2	12424	
z	144	$-3/2 \rightarrow -1/2$ (Upper Set)	-5/2	10132	10374 <sup>±8</sup>
			-3/2	10233	
			-1/2	10319	
			+1/2	10421	
			+3/2	10509	
			+5/2	10591	
z	144	$-3/2 \rightarrow -1/2$ (Lower Set)	-5/2	9378	9598 <sup>±10</sup>
			-3/2	9460	
			-1/2	9545	
			+1/2	9645	
			+3/2	u	
			+5/2	9817	
y	147	$+3/2 \rightarrow +1/2$ (Upper Set)	-5/2	10971	11211 <sup>±6</sup>
			-3/2	11073	
			-1/2	11164	
			+1/2	11257	
			+3/2	11349	
			+5/2	11442	
y	147	$+1/2 \rightarrow -1/2$ (Upper Set)	-5/2	11827	12054 <sup>±3</sup>
			-3/2	11917	
			-1/2	12007	
			+1/2	12100	
			Std.	12188	
			+3/2	u	
+5/2	12284				
x	176	$+1/2 \rightarrow -1/2$	-5/2	11765	11988 <sup>±3</sup>
			-3/2	11853	
			-1/2	11946	
			+1/2	12030	
			+3/2	12119	
			+5/2	12212	

TABLE II (Continued)

Axis	Temp. ( $^{\circ}\text{C}$ )	Transition	m	Line Position	$\lambda_{\text{vac}}$
x	176	+3/2 +1/2	+3/2 +5/2	11103 11196	10968 $\pm$ 8
y	149	+1/2 -1/2 (Upper Set)	-3/2 -1/2	11910 11999	12045 $\pm$ 4
y	149	+3/2 +1/2 (Upper Set)	-1/2 +1/2	11161 11255	11208 $\pm$ 8
y	149	+1/2 -1/2 (Lower Set)	-5/2	11729	11959 $\pm$ 10
y	149	+3/2 +1/2 (Lower Set)	-5/2 -3/2	10610 10701	10840 $\pm$ 20

TABLE IIIPosition of esr Lines in Gauss in Cu: Zn, P, O<sub>7</sub>

Axis	Temp. (°C)	Line Position	H <sub>av</sub>
z	181	10050	9927 <sup>±4</sup>
		9969	
		9884	
		9805	
		12231*	
z	154	10080	9953 <sup>±4</sup>
		9995	
		9911	
		9824	
		12238*	
z	150	10081	9953 <sup>±4</sup> 9926 <sup>±10</sup>
		9996	
		9960	
		9909	
		9882	
		9824	
z	148	12235*	9958 <sup>±4</sup> 9921 <sup>±10</sup>
		10088	
		10002	
		9963	
		9915	
		9885	
		9827	
9790			
z	147	12237*	9961 <sup>±5</sup> 9924 <sup>±10</sup>
		10091	
		10003	
		9920	
		9830	
		9793	
z	145	12237*	9961 <sup>±4</sup> 9928 <sup>±10</sup>
		10092	
		10004	
		9918	
		9877	
		9829	
z	145	9794	9961 <sup>±4</sup> 9928 <sup>±10</sup>
		12233*	

TABLE III (Continued)

Axis	Temp. (°C)	Line Position	How
z	144	10093	
		10012	9967 $\pm$ 6
		9922	9929 $\pm$ 10
		9836	
		9798	
		12238*	
z	142	10097	
		10011	9967 $\pm$ 6
		9922	9930 $\pm$ 10
		9837	
		9790	
		12235*	
z	141	10106	
		10012	9970 $\pm$ 6
		9927	9926 $\pm$ 10
		9834	
		9788	
		12234*	
z	134	10115	
		10026	9982 $\pm$ 3
		9937	9928 $\pm$ 10
		9848	
		9796	
		12241*	
z	133.5	10105	
		10015	9971 $\pm$ 4
		9927	9916 $\pm$ 10
		9842	
		9787	
		12245*	
z	132.5	10172	
		10076	10032 $\pm$ 10
		10029	9915 $\pm$ 6
		9988	
		9951	
		9880	
		9799	
		12244*	

TABLE III (Continued)

Axis	Temp. (°C)	Line Position	Har
z	111	10180	10035±6 9920±8
		10082	
		10035	
		9987	
		9955	
		9885	
		9802	
		12249*	
z	Room	10212	10064±5 9943±7
		10114	
		10060	
		10014	
		9979	
		9906	
		9819	
		12268*	
y	181	11725 12245*	11725±10
y	154	11748 12248*	11748±10
y	134.5	11781 12257*	11781±10
y	109	11785 12259*	11785±10
x	177	11674 12222*	11675±10
x	137	11704 12210*	11704±10
x	121	11645	
		11698	
		11739	
		12214*	
x	Room	11669	
		11723	
		11766	
		12239*	

line positions for the z-axis is equal in magnitude to 2 D within the experimental error. The absolute value of D is obtained directly and yields  $|D| = 1103 \pm 3$  gauss. If this value of D is used, E can be found from the differences between the line positions for the other axes. The procedure followed was to find E from the differences between the  $+5/2 \rightarrow +3/2$  and  $+3/2 \rightarrow +1/2$  line positions for both the x and y-axes. For the x-axis, this difference is

$$946 = D - 3E - \frac{9(D+E)^2}{4 H_0} + 27 \frac{(D-3E)(D+E)^2}{8 H_0^2} \quad (4.1)$$

Again if E is less than 70 gauss the significant terms are

$$946 = D - 3E - \frac{9D^2}{4H_0} - \frac{18DE}{4H_0} + \frac{27D^3}{8H_0^2} - \frac{27D^2E}{8H_0^2} \quad (4.2)$$

Similarly, for the y-axis we have for this difference

$$870 = D+3E - \frac{9D^2}{4H_0} + \frac{18DE}{4H_0} + \frac{27D^3}{8H_0^2} + \frac{27D^2E}{8H_0^2} \quad (4.3)$$

For  $H_0 = 1.22 \times 10^4$  gauss, the values obtained are  $11.0 \pm 2$  and  $11.3 \pm 2$  gauss respectively. In addition the sign of E is found to be opposite to that of D. As a check the  $+1/2 \rightarrow -1/2$  line positions for the x and y-axes were calculated from the average of the  $+3/2 \rightarrow +1/2$  and  $-1/2 \rightarrow -3/2$  line positions, using the above values of D and E. The calculated values agree with the experimental values within experimental error. Finally, the values of  $H_0$  for the three axes were calculated and the g-values found by multiplying the ratio of the standard line position to  $H_0$  by 2.0030, the g-value of the standard sample.

The parameters were determined in the manner described above for temperatures where measurements were made along all three axes. Near the upper transition in the intermediate

temperature range with the z-axis parallel to the magnetic field the low intensity of the signals made interpretation difficult. The situation is considerably better for the y-axis spectra and measurements were made in this region along the y-axis only. Since E was found to be small in all three temperature regions, it was assumed to remain small throughout the entire intermediate region. The D values in this region were obtained from the y-axis data by giving  $E$  its value at 135°C and solving the equation obtained by taking the difference between the  $+3/2 \rightarrow +1/2$  and  $+1/2 \rightarrow -1/2$  line positions. For

$|E| = 5$  gauss and  $H_0 = 1.22 \times 10^4$  gauss the significant terms are

$$H_{+3/2 \rightarrow +1/2} - H_{-1/2 \rightarrow +1/2} = D + 3E - \frac{3D^2}{4H_0} - \frac{33D^3}{8H_0^2} \quad (4.4)$$

This is a cubic equation, but the predominance of the linear term results in convergence on the only physically meaningful solution.

The values of the spin Hamiltonian at temperatures for all three axes are given in table 4. It will be noted from table 2 that the parameters at 136°C were actually obtained from the spectra taken over a range of temperatures from 133 to 137°C. It is only the  $+1/2 \rightarrow -1/2$  spectrum which was recorded at 133°C but since these line positions change very slowly with the temperature the effective temperature range is 135° to 137°C. Over this range D changes by only 1.5 gauss (see figure 14), so that the temperature was assigned at 136°C without contributing significant errors. Also the spectra for the z-axis were measured at a sample temperature of 175°C,

TABLE IV

Spin Hamiltonian Parameters for  $Mn^{++}$  at Room Temperature,  
136°C and 184°C<sup>+</sup>

	184°C	136°C (Upper)	136°C (Lower)	Room Temp.
D	-1103 <sup>±3</sup>	-887 <sup>±4</sup>	-1319 <sup>±5</sup>	-612
E	11 <sup>±2</sup>	7 <sup>±3</sup>	5 <sup>±4</sup>	22
$g_x$	2.0010 <sup>±0.0005</sup>	2.0033 <sup>±0.0010</sup>	2.0018 <sup>±0.0010</sup>	2.0004 <sup>±0.0012</sup>
$g_y$	2.0005 <sup>±0.0005</sup>	2.0025 <sup>±0.0010</sup>	1.9999 <sup>±0.0010</sup>	1.9994 <sup>±0.0012</sup>
$g_z$	2.0017 <sup>±0.0005</sup>	2.0001 <sup>±0.0008</sup>	2.0001 <sup>±0.0008</sup>	2.0019 <sup>±0.0012</sup>
A <sub>x</sub>	-89.6 <sup>±0.5</sup>	-90.0 <sup>±0.8</sup>	-83.4 <sup>±0.8</sup>	-93.6 <sup>±1.2</sup>
A <sub>y</sub>	-89.2 <sup>±0.5</sup>	-90.2 <sup>±1.6</sup>	-85.4 <sup>±1.2</sup>	-92.4 <sup>±1.6</sup>
A <sub>z</sub>	-91.2 <sup>±0.5</sup>	-89.8 <sup>±1.2</sup>	-85.0 <sup>±1.6</sup>	-93.0 <sup>±0.8</sup>

+ The signs of D and E have been assigned on the assumption that A is negative.

about  $10^\circ$  below the corresponding measurements for the x and y-axes. Again it was found that the line positions did not vary appreciably in this region (See, for example, the x-axis line position at  $184^\circ\text{C}$  and  $176^\circ\text{C}$  in table 2). The values of D obtained from y-axis measurements only, as well as those from table 4 are plotted as a function of temperature in figure 14.

Positive and negative signs are assigned in table 4 even though only the relative signs of the parameters can be determined from the data in table 2. As has already been shown the signs of D and E are opposite. In (II, 6) it was shown that the relative signs of D and A could be determined by comparing the intervals between the extreme hyperfine positions of each five structure group. These differences are rather small at the high fields used and only the high temperature data is accurate enough for this purpose. The hyperfine splittings of the five structure groups for the three axes are given in table 5 as well as the differences between successive groups. The average of these differences is  $4.3 \pm 2.2$  gauss. The average difference calculated from equation (2.7) for  $A=90$  gauss and  $H_0 = 1.22 \times 10^4$  gauss is 3.5 gauss. From equations (2.4), (2.5) and (2.7) it can be seen that, for the x and y-axes spectra, if D and A are of the same sign the higher magnetic field fine structure groups should have smaller hyperfine splitting and vice versa if D and A are of opposite sign. Thus the data in table 5 shows

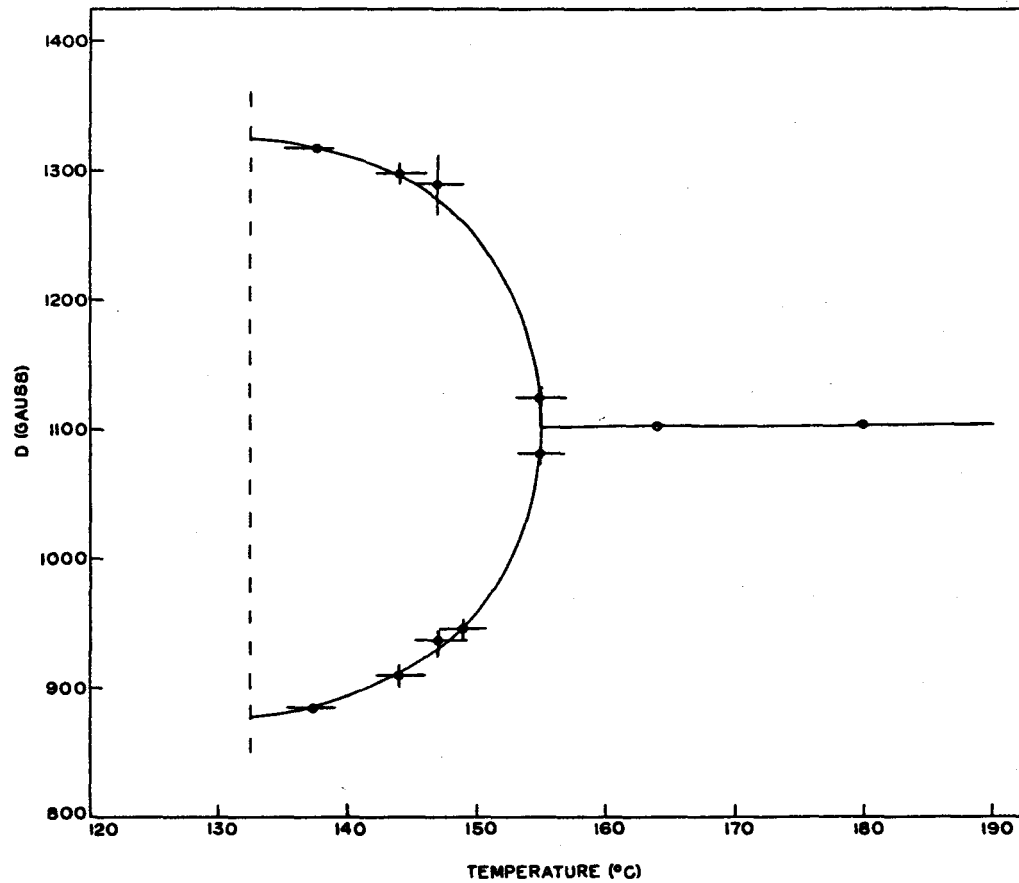


FIG. 14. TEMPERATURE VARIATION OF THE AXIAL SPLITTING PARAMATER FOR  $Mn^{2+}$  IN  $Zn_2BO_7$

TABLE V

Hyperfine Splitting of Fine Structure Lines at 184°C

	x	$\Delta H$	y	$\Delta H$	z	$\Delta H$
$-1/2 \leftrightarrow -3/2$	$442 \pm 4$	$6 \pm 6$	$436 \pm 3$	$4 \pm 5$		
$+1/2 \leftrightarrow -1/2$	$448 \pm 2$	$4 \pm 5$	$440 \pm 2$	$6 \pm 5$	$456 \pm 2$	$2 \pm 5$
$+3/2 \leftrightarrow +1/2$	$452 \pm 3$	$5 \pm 6$	$446 \pm 3$	$3 \pm 6$	$454 \pm 3$	
$+5/2 \leftrightarrow +3/2$	$457 \pm 3$		$449 \pm 3$			

$$\Delta H_{\text{cov}} = 4.3 \pm 2.2$$

$$\Delta H_{\text{calc}} = 3.5$$

D and A to be of like sign. Tables 2 and 5 were prepared with this foreknowledge, although the conclusion is independent of this fact. Finally, the signs of A reported for  $Mn^{++}$  are invariably negative, so A was assumed to be negative in the present case. This means that D is also negative and E is positive. Because of the gradual nature of the changes observed in D and E it can also be inferred that these parameters keep the same sign over the whole range of temperatures.

#### 9. Effects Arising From Changes in the Magnetic Axes Directions

It was stated earlier that the failure in fitting the experimentally determined line positions to equations (2.4) and (2.6) can be used to set a maximum on the possible deviation of the z-axis setting from being parallel to the magnetic field. For an approximate calculation of small angular changes it is sufficient to use only the first order terms in the expressions for the angular variation of the line positions. Also, since E is small only the axially symmetric terms need be considered. Bleaney (1954) has shown that the expression for the angular variation of the fine structure to the first order for the axially symmetric case is

$$H_{m \leftrightarrow m-1} = H_0 + D \left(M - \frac{1}{2}\right) \frac{(3g_{\parallel}^2 \cos^2 \theta - 1)}{g^2} \quad (4.5)$$

where  $\theta$  is the angle between the applied magnetic field and the z-axis and  $g^2 = g_{\parallel}^2 + g_{\perp}^2$ . In the  $Mn^{++}$  case  $g_{\parallel}^2 < g_{\perp}^2$  so

that the term containing the angular dependence is  $D(M-1/2)$   $(3\cos^2\theta-1)$ . For example, for  $M = 3/2$ , the difference between this term for  $\theta = 0^\circ$  and  $\theta = 5^\circ$  is  $0.024D$ , and for  $\theta = 90^\circ$  and  $\theta = 85^\circ$  is  $0.022D$ . Thus if a measurement is made at  $\theta = 5^\circ$  and  $D$  determined from equation (4.5) with  $\theta$  set equal to zero, the value found for  $D$  will be  $0.012 D$  less than its proper value. If now  $H_{M \leftrightarrow M-1} - H_0$  is determined by experiment for  $\theta = 85^\circ$  it will be found to have a value less than its value at  $\theta = 90^\circ$  by an amount  $0.022 D$ . Thus the two sides of equation (4.1) will differ by an amount  $0.010 D$ . To complete the analogy with the procedure followed in section (IV, 8), it is necessary to also evaluate  $H_{M \leftrightarrow M-1} - H_0$  at right angles to both the  $\theta = 5^\circ$  and  $\theta = 85^\circ$  directions considered previously, that is at  $\theta = 90^\circ$ . In this case equation (4.5) fails to balance by an amount of  $0.012 D$ . By inspection of equations (4.2) and (4.3) it can be seen that these two effects will always add in producing different values of  $E$  from these two equations. Equations (4.2) and (4.3) are actually the differences between the  $+5/2 \rightarrow +3/2$  and  $+3/2 \rightarrow +1/2$  line positions, but the first two terms on the right hand side are the same for the intervals between the  $+3/2 \rightarrow +1/2$  and  $+1/2 \rightarrow -1/2$  line positions. The remaining terms on the RHS are small enough that changes in them may be ignored. Thus the variation in  $E$  determined by this method is  $0.022 D$  if the  $z$ -axis is misset by  $5^\circ$ .

3

The two values of  $E$  obtained for the lower set of

lines at  $136^\circ$  were  $1 \pm 4$  and  $8 \pm 4$ . Although the relatively large uncertainties of the two values overlap, they also allow as large a value of  $\theta$  as  $6^\circ$ . The values of  $E$  for the upper set of lines are  $6 \pm 3$  and  $7 \pm 3$  gauss, which limits  $\theta$  to  $5^\circ$  for  $D = 887$  gauss. For the room temperature results the values are  $18 \pm 3$  and  $26 \pm 3$ . The value of  $9^\circ$  for  $\theta$  needed to span the range from 15 to 29 for  $E$  also sets an upper limit on the error in the measured value of  $D$  of +29 gauss, so that  $D$  is between 607 and 646 gauss.

#### 10. The Spin Hamiltonian Parameters for $\text{Cu}^{++}$

The computation of the spin Hamiltonian parameters is a much easier task for  $\text{Cu}^{++}$  than for  $\text{Mn}^{++}$ . Second order hyperfine effects are small for the large magnetic fields used (Bleaney, Bowers, and Ingram, 1955) so that the  $g$ -values can be determined by taking the center of the hyperfine group as the fine line position. The parameters are presented in table 6 for high and intermediate temperatures. The value of  $A_z$  is missing for one site at  $136^\circ\text{C}$  because only one line could be resolved. The room temperature parameters were not computed because of the difficulty in labelling the different sets of lines. One noteworthy feature of the room temperature spectra is that  $A_z$  is at least  $98 \pm 2$  gauss for one of the sites. It can be seen in table 4 that the hyperfine splitting for  $\text{Mn}^{++}$  is also appreciably larger at room temperature. Finally, the splitting between the two sites which appear in the  $\text{Cu}^{++}$

TABLE VISpin Hamiltonian Parameters for  $\text{Cu}^{++}$  at  $136^\circ\text{C}$  and  $181^\circ\text{C}$ 

	181°C	136°C	
$g_x$	$2.097 \pm 0.002$	$2.089 \pm 0.004$	$2.089 \pm 0.004$
$g_y$	$2.092 \pm 0.002$	$2.084 \pm 0.004$	$2.084 \pm 0.004$
$g_z$	$2.468 \pm 0.002$	$2.456 \pm 0.002$	$2.471 \pm 0.004$
$ A_x ,  A_y $	<15 gauss	<15	<15
$ A_z $	$82 \pm 2$ gauss	$89 \pm 3$	

z-axis spectra is plotted as a function of temperature in figure 15.

### 11. The Directions of the Magnetic Axes in the Crystal

One of the magnetic axes must lie along the crystalline two-fold axis in  $\beta$ - $\text{Zn}_2\text{P}_2\text{O}_7$ . The z-axis would normally lie along the long axis of the octahedron but since the octahedron is so distorted in this case it was decided to confirm this. A sample of Cu doped  $\text{Zn}_2\text{P}_2\text{O}_7$  was aligned by esr on the 3 cm. sample holder described in section (IV, 2), and the directions for which the x and z magnetic axes were parallel to the magnetic field were noted. The sample holder and sample were then removed from the magnetic field and the directions of some prominent faces of the sample were determined optically. It was found that one of these faces was about  $4^\circ$  from being parallel to the magnetic z-axis. Since the accuracy of each measurement was about  $\pm 2^\circ$  it seems likely that this is a real difference. X-ray measurements showed that this face corresponded to the  $(10\bar{1})$  face in the  $\beta$ - $\text{Zn}_2\text{P}_2\text{O}_7$  or to the  $(60\bar{2})$  in the  $\alpha$ -phase, confirming that the magnetic z-axis is  $4^\circ \pm 4^\circ$  away from the long axis of the octahedron.

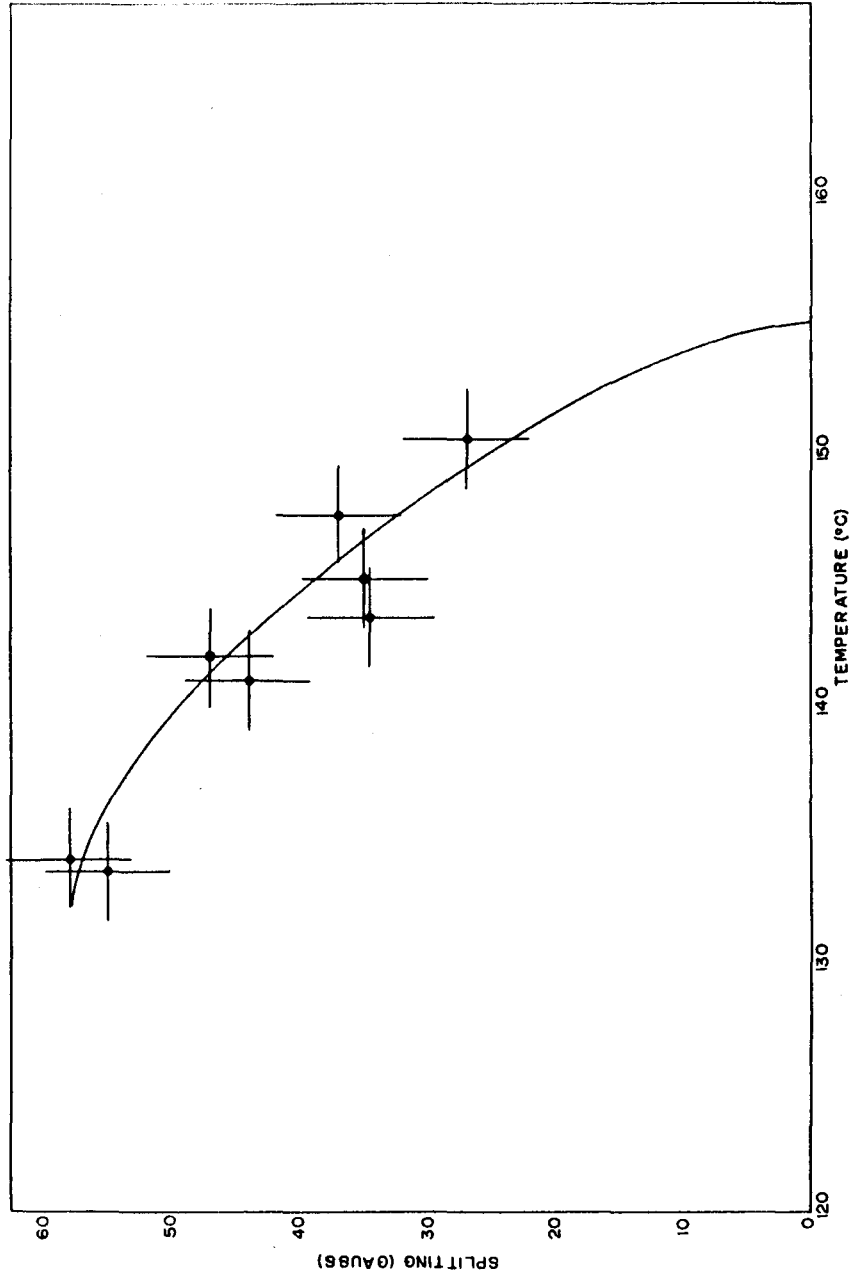


FIG. 15. TEMPERATURE VARIATION OF THE SPLITTING OF THE  $\text{Cu}^{++}$  SPECTRA WITH  $H//Z$

## CHAPTER V

### DISCUSSION OF RESULTS AND CONCLUSIONS

#### 1. The Relation Between the Electric Field Gradient and the Axial Splitting Parameter D

The paucity of good crystallographic data for systems where  $Mn^{++}$  substitutes for a divalent cation in a noncubic environment has prevented a critical study of the relation between the electric field gradient and the axial splitting parameter. In the non-hydrated compounds studied by esr the symmetry of the  $Mn^{++}$  spectrum is usually cubic and in the hydrated compounds the hydrogen positions are, in general, not known. In addition the fact that the experimental values of  $|D|$  for  $Mn^{++}$  with one exception (Donovan and Vuylsteke, 1962), have been less than 400 gauss in comparison to the much larger range of results available for  $Fe^{3+}$  would tend to discourage such a study. The results presented in chapter IV extend this range considerably and are obtained in a material for which the atom positions are being accurately determined.

It will be seen later that among the divalent phosphates the most useful for a comparison of  $D$  and  $A^{\circ}_2$  for  $Mn^{++}$  are  $Zn_2P_2O_7$  and  $Mg_2P_2O_7$ . Since only the  $\beta$ - $Zn_2P_2O_7$  structure has been completely determined, this comparison is not yet possible.

It would be profitable at this stage, however, to do some preliminary calculations to investigate the behaviour of the lattice sums involved in the field gradient computation as a function of distance from the site concerned and also to compare the calculated field gradients in  $\beta$ - $\text{Zn}_2\text{P}_2\text{O}_7$  to that in the isostructural  $\text{Mn}_2\text{P}_2\text{O}_7$ . This information would be useful for a number of reasons. The contributions from the neighbouring oxygens would give some indication of the magnitude of effects arising from possible distortions of the lattice and also of the order of magnitude of the displacements necessary to give rise to the variation in D in the intermediate temperature region shown in figure 14.

The details of the field gradient calculations are presented in appendix 2. The oxygen ions are characterized by a charge of  $-2e$ , the zinc ions by  $+2e$ , and the phosphorus ions by  $+5e$ , where  $e$  is the absolute value of the electronic charge. This approximation will be discussed below. For  $\beta$ - $\text{Zn}_2\text{P}_2\text{O}_7$ , considering the octahedron of oxygens alone, the field gradient is  $-0.082e$  (in units of  $(1/\text{Å}^3)$ ). When the six nearest phosphorus ions are included the total changes to  $-0.110e$  and the next thirteen atoms that contribute most significantly bring the total to  $-0.148e$ . This slow convergence of the field gradient calculations has already been pointed out by Bersohn (1958) and calculations of this sort are usually carried out to include a sphere of radius about five lattice

constants. From a computational point of view this is a disadvantage, but it has the advantage that it tends to suppress the effect of local distortions near the impurity ion. Only the contributions of the nearest neighbours are considered in the  $\text{Mn}_2\text{P}_2\text{O}_7$  calculations, but the value of  $-0.050e$  compared with that of  $-0.082e$  for  $\beta\text{-Zn}_2\text{P}_2\text{O}_7$  demonstrates the order of the uncertainty in the field gradient when  $\text{Mn}^{++}$  is an impurity in  $\beta\text{-Zn}_2\text{P}_2\text{O}_7$ . It is still an open question as to the degree to which the structure adjusts to a substitutional impurity. Results of these calculations also reinforce the point made above that it would be advisable to restrict the calculations to cases where the  $\text{Mn}^{++}$  ion is substituting for  $\text{Mg}^{++}$  or  $\text{Zn}^{++}$ , since the average cation oxygen distances are within  $0.05\text{\AA}$  of being the same in many isostructural compounds.

One other question which arises in these calculations concerns the validity of the ionic charge model. Pauling's (1960) electroneutrality principle states that the net charges on ions of stable complexes are smaller than their valence numbers. Cruickshank (1962) has applied Pauling's electronegativity relations to  $\text{Sc}_2\text{Si}_2\text{O}_7$ , an isostructure of  $\beta\text{-Zn}_2\text{P}_2\text{O}_7$  and deduced ionic charges reduced by more than a factor of two from their formal values, but he admits that these considerations are still in the speculative stage. In general this charge neutralization would tend to lower the magnitude of the crystalline electric field, but since the reduction is not the same for each ion the effect on the electric field

will be quite complicated. Although these effects may be quite important, they might also be expected to be of a similar nature in isostructural compounds. Thus a comparison of  $D$  and  $A_2^\circ$  in the various phases of  $Zn_2P_2O_7$  and  $Mg_2P_2O_7$  could yield values of  $C_1$  and  $C_2$  in the equation  $D = C_1 Vax + C_2 Vax^2$ . In the event charge reduction estimates are unduly pessimistic,  $D$  and  $A^\circ$  values for the orthophosphates would also be useful. Preliminary experiments with both  $Mg_2P_2O_7$  and  $\beta$ - $Zn_3(PO_4)_2$  have shown that  $D$  is of the same order of magnitude in these crystals as in  $\beta$ - $Zn_2P_2O_7$ , and accurate measurements are in progress.

## 2. The Intermediate Phase

The most interesting result of this study is the variation of the  $D$  value in the temperature range from  $132^\circ C$  to  $155^\circ C$ . This variation suggests a gradual change of the average atomic positions as the temperature is lowered, beginning at  $155^\circ C$ . There is no detectable discontinuity in the variation from this temperature to  $132^\circ C$ . In confirmation of this behavior, figure 15 shows the variation in the difference between the average line positions of the two sets of lines, which begin to appear in the  $Cu^{++}$  spectra at about  $155^\circ C$ . Although the resolution of the splitting is not as high as that in the  $Mn^{++}$  spectra, the curve extrapolates to zero at about  $155^\circ C$ . This indicates that this sort of behavior is not merely a peculiarity of the  $Mn^{++}$  impurity, but

is characteristic of the host crystal.

One striking feature of the  $Mn^{++}$  spectra is the broadening which occurs near  $155^{\circ}C$ . For the  $+\frac{1}{2} \leftrightarrow -\frac{1}{2}$  electronic transition this broadening is not obvious. However, it is quite pronounced for the  $\pm 3/2 \leftrightarrow \pm 1/2$  transitions and even more so for the  $\pm 5/2 \leftrightarrow \pm 3/2$  transitions. Equations (2.4) show that the  $+\frac{1}{2} \leftrightarrow -\frac{1}{2}$  line positions depend only slightly on  $D$ , in contrast to the line positions of the other transitions. This suggests that the broadening is due to lattice vibrations rather than to lifetime effects, since the latter would be expected to introduce equal broadening of all transitions. Unfortunately the broadening prevents definite assignment of the total signal below  $155^{\circ}C$  to the two sites which appear at this temperature. If the change at  $155^{\circ}C$  is a true phase transition and the system is in equilibrium then the Gibbs phase rule precludes the existence of the high temperature phase in this region. The definite appearance of a new and different esr spectrum in this region in both the case of  $Mn^{++}$  and of  $Cu^{++}$  argues for a distinct phase. If this is so, the apparent lack of latent heat in the differential thermal analysis experiments (Katnack and Hummel, 1955) and the gradual change of the spectra indicate that the transition at  $155^{\circ}C$  is of second order. Certainly, careful specific heat measurements around  $155^{\circ}C$  are desirable in order to substantiate the proposed thermodynamic order for the transition and to compare the breadth of the specific heat anomaly with the

range of line broadening noted in the esr spectra.

The extinctions in the x-ray diffraction patterns of  $\text{Zn}_2\text{P}_2\text{O}_7$  above  $132^\circ\text{C}$  are consistent with the C-2/m, C-2, or C-m space groups. In general one must attempt a structure resolution in each of these space groups before the proper space group can be chosen. The existence of only one esr site for  $\text{Mn}^{++}$  in the  $\beta$ -phase is consistent with and provides direct evidence for the space group C-2/m chosen for the structure above  $155^\circ\text{C}$ . In the intermediate phase two esr sites are detected but the extinctions, the unit cell geometry and the intensities of the individual x-ray reflections appear unchanged. Under the assumption that the appearance of the two sites represents a cooperative change in the host structure the space group symmetry must have been lowered to either C-2 or C-m. Since the esr results indicate that there is a slight shift in the magnetic y-axis of one of the two sites away from the direction of the two fold axis in the  $\beta$ -phase, the C-2 space group is ruled out, so the symmetry of the intermediate phase is C-m.

The fact that the intensities appear unchanged suggest relatively small atomic displacements. This is not inconsistent with the large difference in D values found for the two sites in the intermediate phase since a change by as little as  $0.02\text{A}^\circ$  in the Z-component and the  $\gamma$  value of  $0_3$  (appendix 2) changes the field gradient by about 14% of the total contribution of the nearest 25 ions.

It is difficult to go further in discussing the atomic positions in the intermediate phase without more information. The most tantalizingly suggestive feature of the data in this region is the symmetry of the D value displacements from the high temperature value as illustrated in figure 14. However, there are many possible changes in ion positions which would be capable of giving rise to effects of this order. A knowledge of the dependence of D on the field gradient in this region of D values would be helpful in this respect. Also, the resolution of the  $\alpha$ - $\text{Zn}_2\text{P}_2\text{O}_7$  structure could be very helpful. For example, one would know whether the  $\text{P}_2\text{O}_7^{-4}$  ion bends and whether the central oxygen remains equidistant from the phosphorus atom. An esr study of the transition in  $\text{Mg}_2\text{P}_2\text{O}_7$  will supplement the x-ray study and might provide clues as to the mechanism that applies to the phase transitions in these divalent pyrophosphates. A preliminary experiment on  $\text{Mg}_2\text{P}_2\text{O}_7:\text{Cu}$  showed only one esr site as expected in the C-2/m space group chosen for this phase. No splitting of the esr spectra lines was observed on either side of the transition. The unit cell and the space group of  $\alpha$ - $\text{Mg}_2\text{P}_2\text{O}_7$  have been determined and early progress made on the resolution of the structure. (C. Calvo, to be published) The space group is unambiguously P-2<sub>1</sub>/a and supports as many as 8 different esr sites. The atomic displacement of the Mg, for example, are of the order of  $\frac{1}{4}\text{A}^\circ$  from their high temperature positions. The

esr spectra of  $\text{Mg}_2\text{P}_2\text{O}_7$ : Mn will also be examined around the transition since  $\text{Mn}^{++}$  provides a more sensitive probe for small ionic displacements.

### 3. The Parameters A and g

The g-factors and hyperfine constants for  $\text{Mn}^{++}$  given in Table IV do not show any anisotropy within the experimental error. The only systematic variation in the spin-Hamiltonian parameters seems to be the increase in the hyperfine splitting factor A as the axial splitting D decreases. Any functional relationship does not appear to be of a simple form. Although it is difficult to see any significance in the trend, the fact that the two A values given for  $\text{Cu}^{++}$  in Table VI show a parallel trend suggests that a basis for this correlation may be found in future theoretical studies. Therefore it is worthwhile to note these effects.

### 4. Further Experiments

It has been pointed out above that more structural and esr data on  $\text{Zn}_2\text{P}_2\text{O}_7$  and  $\text{Mg}_2\text{P}_2\text{O}_7$  are required for a comparison of D and A. Although only a magnet with six inch diameter pole pieces has been available to date, it is hoped that a twelve inch magnet will be available for some of the proposed experiments. This would allow sufficient space in the magnetic field to provide facilities for rotation of the sample with respect to the magnet field direction about two mutually perpendicular axes and thus allow the directions of

the magnetic axes to be determined in those cases where none of the axes directions can be determined from symmetry considerations.

As for the transitions themselves, in addition to the esr study of  $\text{Mg}_2\text{P}_2\text{O}_7:\text{Mn}$  mentioned above, NMR studies of the phosphorus ions in  $\text{Mg}_2\text{P}_2\text{O}_7$  and  $\text{Mg}_2\text{P}_2\text{O}_7$  similar to those carried out in  $\text{Li Mn PO}_4$  (Mays, 1963) should be quite informative.

## APPENDIX I

### FOURTH ORDER PERTUBATION CONTRIBUTIONS TO THE ENERGY LEVELS OF THE SPIN HAMILTONIAN FOR $Mn^{++}$

Since the electronic and the nuclear parts of the spin Hamiltonian (2.6) may be diagonalized separately, the second two terms on the RHS of equation (2.6) can be considered a perturbation on the first term and the last term can be neglected for the purposes of calculating the electronic energy levels. Thus one has

$$H = H_0 + H_1$$

$$\text{where } H_1 = DS_z^2 + E(Sx^2 - Sy^2)$$

The fourth order terms are given by

$$B_4^n = \sum_{n'}^{n' \neq n} \langle \alpha^n | H_1 | \alpha^{n'} \rangle \{ \alpha^{n'} | 3^n \} - B_2^n \{ \alpha^n | 2^n \} \quad (A1.1)$$

(Condon and Shortly, 1935), where

$$\{ \alpha^{n'} | 3^n \} = \sum_{\lambda=1}^2 B_\lambda^n \frac{\{ \alpha^{n'} | (3-\lambda)^n \}}{\alpha^{n'} - \alpha^n} + \sum_{n''} \frac{\langle \alpha^{n'} | H_1 | \alpha^{n''} \rangle \{ \alpha^{n''} | 2^n \}}{\alpha^n - \alpha^{n'}}$$

$$\{ \alpha^{n'} | 2^n \} = - \frac{\langle \alpha^{n'} | H_1 | \alpha^n \rangle \langle \alpha^n | H_1 | \alpha^{n'} \rangle}{(\alpha^{n'} - \alpha^n)^2} - \sum_{n''} \frac{\langle \alpha^{n'} | H_1 | \alpha^{n''} \rangle \{ \alpha^{n''} | 1^n \}}{\alpha^{n'} - \alpha^n}$$

$$\{ \alpha^{n'} | 1^n \} = \frac{\langle \alpha^{n'} | H_1 | \alpha^n \rangle}{\alpha^n - \alpha^{n'}}$$

$$\{ \alpha^n | 2^n \} = \frac{1}{2} \sum_{n'} |\{ \alpha^{n'} | 1^n \}|^2$$

$$\{ \alpha^n | 1^n \} = 0$$

$$B_2^n = \sum_{n'} \frac{\langle \alpha^n | H | \alpha^{n'} \rangle \langle \alpha^{n'} | H | \alpha^n \rangle}{\alpha^n - \alpha^{n'}}$$

$$B_1^n = \langle \alpha^n | V | \alpha^n \rangle$$

The non-zero matrix elements are given in table 7 for the magnetic field parallel to the magnetic z-axis. Substituting the appropriate matrix elements in equation (A1.1) leads to

$$\begin{aligned} \beta_4^{\pm 5/2} &= \pm 45 \frac{D^2 E^2}{H_0^3} \mp \frac{5}{4} \frac{E^4}{H_0^3} \\ \beta_4^{\pm 3/2} &= \pm 9 \frac{D^2 E^2}{H_0^3} \mp 117 \frac{E^4}{H_0^3} \\ \beta_4^{\pm 1/2} &= \mp 36 \frac{D^2 E^2}{H_0^3} \mp 28 \frac{E^4}{H_0^3} \end{aligned} \quad (\text{A1.2})$$

The fourth order terms to be added to the expressions for the line positions for H//z are thus

$$\begin{aligned} \pm 5/2 \leftrightarrow \pm 3/2 : & \quad + 36 \frac{D^2 E^2}{H_0^3} + 28 \frac{E^4}{H_0^3} \\ \pm 3/2 \leftrightarrow \pm 1/2 : & \quad + 45 \frac{D^2 E^2}{H_0^3} - \frac{5}{4} \frac{E^4}{H_0^3} \\ +1/2 \leftrightarrow -1/2 : & \quad + 72 \frac{D^2 E^2}{H_0^3} + 56 \frac{E^4}{H_0^3} \end{aligned} \quad (\text{A1.3})$$

The fourth order perturbation terms for H//x and H//y are obtained by making the substitutions given in equations (2.5).

TABLE VII

VALUES OF THE MATRIX ELEMENTS  $\langle \alpha^n | H | \alpha^n \rangle$

$\begin{matrix} n \\ n' \end{matrix}$	+ 5/2	+ 3/2	+ 1/2	-1/2	-3/2	-5/2
+ 5/2	$(5/2)^2 D$		$\sqrt{10} E$			
+ 3/2		$(3/2)^2 D$		$\sqrt{18} E$		
+ 1/2	$\sqrt{10} E$		$(1/2)^2 D$		$\sqrt{18} E$	
- 1/2		$\sqrt{18} E$		$(1/2)^2 D$		$\sqrt{10} E$
- 3/2			$\sqrt{18} E$		$(3/2)^2 D$	
- 5/2				$\sqrt{10} E$		$(5/2)^2 D$

APPENDIX VIII

FIELD GRADIENT CALCULATIONS

The electric field gradient (f.g.) at a lattice site in a crystal can be written

$$\text{f.g.} = \sum_i e_i \frac{3z_i^2 - r_i^2}{r_i^5} = \left(\frac{5}{\pi}\right)^{1/2} A_2^o \quad (\text{A2.1})$$

where  $r_i$  is the distance to the  $i$ th neighbour, which has a component along the  $z$  axis  $z_i$  and is characterized by the charge  $e_i$ . The series represented by equation (A2.1) converges slowly but a program for the IBM 704 is available on cards which calculates the f.g. in an arbitrary direction for a crystal of arbitrary space group (Bersohn, 1958). However, the calculations below are intended merely to illustrate some arguments in chapter V and only include a small number of neighbours.

The coordinates of the ions considered for  $\beta\text{-Zn}_2\text{P}_2\text{O}_7$  are given in table 8. All of these except  $\text{Zn}_1$  are related by the two-fold axis to a similar ion which makes an equal contribution to the f.g. The  $z$ -axis is taken to be the 0 direction. Table 9 gives the results of the calculations. The quantity  $q$  is the charge assigned to each ion and  $e$  is the absolute value of the electronic charge. The last column of table 9 gives the contribution of the ion in question to the f.g. as well as that of the ion related to it by the two fold axis.

The analogous quantities for  $\text{Mn}_2\text{P}_2\text{O}_7$  are given in table 10 and 11.

TABLE VIIIATOM POSITIONS IN  $\beta$ -Zn<sub>2</sub>P<sub>2</sub>O<sub>7</sub>

	a	b	c
O <sub>1</sub>	+0.826	1.575	+1.284
O <sub>2</sub>	1.573	-1.285	.904
O <sub>3</sub>	1.732	.290	-.904
O <sub>4</sub>	0	-2.574	-2.260
O <sub>5</sub>	0	5.716	2.260
O <sub>6</sub>	3.305	1.570	-2.260
O <sub>7</sub>	3.305	1.570	2.260
P <sub>1</sub>	1.917	1.571	-1.772
P <sub>2</sub>	1.917	1.571	2.748
P <sub>3</sub>	1.388	-2.574	1.772
P <sub>4</sub>	1.388	-2.574	-2.748
Zn <sub>1</sub>	0		
Zn <sub>2</sub>	3.305	3.090	0

TABLE IXFIELD GRADIENTS IN  $\beta$ -Zn<sub>2</sub>P<sub>2</sub>O<sub>7</sub>

	Z (A°)	r (A°)	q	$\frac{(3z^2 - r^2)q}{r^5}$
O <sub>1</sub>	-0.056	2.062	-2e	+0.228e
O <sub>2</sub>	-0.864	2.048	-2e	+0.108e
O <sub>3</sub>	-2.151	2.174	-2e	-0.377e
O <sub>4</sub>	1.423	3.425	-2e	+0.048e
O <sub>5</sub>	1.423	6.147	-2e	+0.014e
O <sub>6</sub>	4.436	4.861	-2e	-0.052e
O <sub>7</sub>	1.815	3.965	-2e	+0.020e
P <sub>1</sub>	0.967	3.285	+5e	+0.426e
P <sub>2</sub>	0.423	3.303	+5e	-0.286e
P <sub>3</sub>	0.595	3.224	+5e	-0.168e
P <sub>4</sub>	2.602	4.257	+5e	+0.016e
Zn <sub>1</sub>	0	3.142	+2e	-0.064e
Zn <sub>2</sub>	2.282	4.525	+2e	-0.010e

TABLE XATOM POSITIONS IN  $\text{Mn}_2\text{P}_2\text{O}_7$ 

	a	b	c
$O_1$	-0.829	1.656	-1.289
$O_2$	1.578	-1.321	.944
$O_3$	1.737	.403	-.944

TABLE XIFIELD GRADIENTS IN  $\text{Mn}_2\text{P}_2\text{O}_7$ 

	Z ( $\text{A}^\circ$ )	r ( $\text{A}^\circ$ )	q	$\frac{(3z^2 - r^2)q}{r^5}$
$O_1$	0.043	2.150	-2e	+0.402e
$O_2$	.831	2.115	-2e	+0.226e
$O_3$	2.104	2.188	-2e	-.678e

REFERENCES

- Abragam, A. Phys. Rev. 79 534 (1950)
- Bersohn, R. J. Chem. Phys. 29 362 (1958)
- Bleaney, B. Phil. Mag. 42 441 (1954)
- Bleaney, B., Bowers, K. D. and Ingram, D. J. E. Proc. Roy. Soc. 228 147 (1955)
- Bowers, K. D. and Owen, J. Repts. Prog. Phys. 18 304 (1955)
- Calvo, C. J. Phys. Chem. Solids 24 141 (1963)
- Condon, E. U. and Shortly, G. H., The Theory of Atomic Spectra, Cambridge University Press, London (1935)
- Cruickshank, D. W. J., Acta. Cryst. 15 491 (1962)
- Donovan, R. E. and Vuylsteke, A. A. Phys. Rev. 127 76 (1962)
- Gabriel, J. R., Johnston, D. F. and Powell, M. J. D. Proc. Roy. Soc. (London) 264 503 (1961)
- Germanier, A. M., Gainon, D. and Lecroix, R. Phys. Letters 2 105 (1962)
- Griffith, J. S. The Theory of Transition Metal Ions Cambridge University Press, London (1961)
- Heine, V. Phys. Rev. 107 1002 (1957)
- Ingram, D. J. E. Nature 174 797 (1954)
- International Tables for X-Ray Crystallography, Volume I, Kynoch Press, Birmingham, England (1952)
- Katnack, F. L. and Hummel, F. A. J. Electrochem Soc. 105 125 (1955)
- Lecroix, R. and Emch, G. Helv. Phys. Acta 35 592 (1962)
- Low, W. Solid State Physics Supplement 2 Academic Press, New York (1960)

- Lukaszewicz, K. and Smajkiewicz, R. *Roczniki Chem.* 35 1167 (1961)
- Marshall, W. and Stuart, R. *Phys. Rev.* 123 2048 (1961)
- Mays, J. M. *Phys. Rev.* 131 38 (1963)
- Nicholson, W. J. and Burns, G. *Phys. Rev.* 129 2490 (1963)
- Owens, J. *Proc. Roy. Soc. (London)* A227 183 (1954)
- Pauling, L. *The Nature of the Chemical Bond*, Cornell University Press, Ithica, N.Y. (1960)
- Pieczonka, W. A. Masters Thesis, McMaster University, Hamilton, Ontario (1957)
- Pieczonka, W. A. Ph.D. Thesis, McMaster University, Hamilton, Ontario (1960)
- Pratt, G. W. Jr. and Coelho, R. *Phys. Rev.* 116 281 (1959)
- Pryce, M. H. L. *Phys. Rev.* 80 1107 (1950)
- Ranby, P. W., Mash, D. H. and Henderson, S. T. *Brit. J. Appl. Phys., Supplement 4*, 518 (1955)
- Rei, D. K. *Soviet Phys., Solid State* 3 1613 (1962)
- Rieman, W., Neuss, J. D. and Naiman, B. *Quantitative Analysis*, McGraw-Hill Book Co. Inc. New York and London (1942)
- Roy, R., Middlesworth, E. T. and Hummel, F. A. *Am. Mineral* 33 458 (1948)
- Schuster, N. A. *Rev. Sci. Inst.* 22 254 (1951)
- Stevens, K. W. H. *Proc. Roy. Soc. (London)* A219 542 (1953)
- Stout, J. W. *J. Chem. Phys.* 31 709 (1959)
- Tinkham, M. *Proc. Roy. Soc. (London)* A236 535 (1956)
- Van Vleck, J. H. *Phys. Rev.* 41 208 (1932)
- Watanabe, H. *Progr. Theoret. Phys.* 18 405 (1957)
- Watanabe, H. *Bull. Am. Soc.* 8 439 (1963)
- Wood, J. H. and Pratt, G. W. *Phys. Rev.* 107 995 (1957)

Yakozawa, Y. and Kazumata, Y. J. Phys. Soc. Japan 16 694 (1961)

Zaripov, M. M., Murtazin, Sh. F. and Stepanov, I. V. Opt. Spectry, XIV 224 (1963)

Zavoisky, E. Jour. Phys. U.S.S.R. 9 211 (1945)